AD_____

AWARD NUMBER: W81XWH-05-1-0108

TITLE: Non-Invasive Markers of Tumor Growth, Metastases, and Sensitivity to Anti-Neoplastic Therapy

PRINCIPAL INVESTIGATOR: Jason A. Koutcher

CONTRACTING ORGANIZATION: Memorial Sloan Kettering Cancer Center
New York, NY 10021

REPORT DATE: January 2009

TYPE OF REPORT: Annual

PREPARED FOR: U.S. Army Medical Research and Materiel Command
Fort Detrick, Maryland 21702-5012

The views, opinions and/or findings contained in this report are those of the author(s) and should not be construed as an official Department of the Army position, policy or decision unless so designated by other documentation.

REPORT DOCUMENTATION PAGE

1. REPORT DATE	2. REPORT TYPE	3. DATES COVERED
1 January 2009	Annual	6 Dec 2007 – 5 Dec 2008

4. TITLE AND SUBTITLE

Non-Invasive Markers of Tumor Growth, Metastases, and Sensitivity to Anti-Neoplastic Therapy

5a. CONTRACT NUMBER

5b. GRANT NUMBER
W81XWH-05-1-0108

5c. PROGRAM ELEMENT NUMBER

6. AUTHOR(S)

Jason A. Koutcher

E-Mail: kotuchej@mskcc.org

5d. PROJECT NUMBER

5e. TASK NUMBER

5f. WORK UNIT NUMBER

7. PERFORMING ORGANIZATION NAME(S) AND ADDRESS(ES)

Memorial Sloan Kettering Cancer Center
New York, NY 10021

8. PERFORMING ORGANIZATION REPORT NUMBER

9. SPONSORING / MONITORING AGENCY NAME(S) AND ADDRESS(ES)
U.S. Army Medical Research and Materiel Command
Fort Detrick, Maryland 21702-5012

10. SPONSOR/MONITOR'S ACRONYM(S)

11. SPONSOR/MONITOR'S REPORT NUMBER(S)

12. DISTRIBUTION / AVAILABILITY STATEMENT
Approved for Public Release; Distribution Unlimited

13. SUPPLEMENTARY NOTES

14. ABSTRACT
The goals of this application are to develop methods to non-invasively differentiate fast and slow growing (or aggressive vs. less aggressive) prostate tumors and also develop methods to evaluate response to anti-angiogenic agents. Validation of the results of the treatment studies will be based on tumor growth, metastases, and microvessel density measurement. To date, we have demonstrated that the R3327AT rat prostate tumor which is relatively radiation resistant has detectable lactate which is heterogeneously distributed once the tumor exceeds 600mm3. In contrast, the radiation sensitive, slow growing Dunning H does not have lactate that is detectable by NMR. DCE-MRI studies do not suggest differences in vascular parameters between slow and fast growing rat prostate tumors. The R3327AT tumor was shown to respond to anti-angiogenic therapy which could be predicted based on changes in lactate that were measured with 24 hours of starting treatment.

15. SUBJECT TERMS
NMR, prostate cancer, lactate, vascular permeability

16. SECURITY CLASSIFICATION OF:			17. LIMITATION OF ABSTRACT	18. NUMBER OF PAGES	19a. NAME OF RESPONSIBLE PERSON USAMRMC
a. REPORT	**b. ABSTRACT**	**c. THIS PAGE**			**19b. TELEPHONE NUMBER** *(include area code)*
U	U	U	UU	75	

Table of Contents

Introduction

The primary goal of this study is to determine whether non-invasive magnetic resonance (MR) techniques can distinguish between slow and rapidly growing and metastatic prostate tumors. This is particularly important in prostate cancer where 30% of men over the age of 50 have prostate cancer at autopsy but only 10% of men develop prostate cancer. Reliable methods do not exist to determine which cancers are aggressive and need to be treated vs. patients who could undergo watchful waiting. A second goal is to determine if anti-angiogenesis agents can be used as chronic low toxicity therapy for "newly diagnosed" tumors and as adjuvant to "curative" therapies and if MR techniques can be used as an early or *a priori* marker of tumor response. We propose that non invasive measurements of tumor vascular volume, permeability, choline and lactate will predict tumor aggressiveness (growth rate, tendency to metastasize). The hypothesis is based on data which indicates that tumor growth rates and metastases are related to angiogenesis which can be detected by dynamic contrast enhanced magnetic resonance imaging (DCE-MRI).

In addition, we propose to determine whether chronic anti-angiogenic therapy can be used in small "newly diagnosed" tumors and as an adjuvant to radiation. It will also be determined whether MRSI and DCE-MRI can predict response to anti-angiogenic therapy. We will also study the effect of anti-angiogenic therapy in small "newly diagnosed" tumors and also as an adjuvant post radiation to determine if it delays tumor growth and metastases. Tumor doubling times and number of metastatic lesions in the lung will be the biological outcome measures. Developing chronic treatment modalities that delay (or obviate) the need for radical therapy will enhance treatment of prostate cancer and possibly quality of life. Similarly, developing a treatment that enhances response to radiation could potentially enhance the cure rate or delay recurrence which might alter subsequent therapy. The techniques applied here are available or readily implemented on clinical scanners (choline and lactate detection; DCE-MRI) so the research is highly translational.

Body

Data Presentation: Biological

A. Data acquisition (does not differ significantly from last year's report):

For MR studies, tumor bearing rats were anesthetized with isoflurane (1.0-2.5%) and compressed air. A 24 gauge tail vein catheter (Terumo Medical Corporation, Elkton, MD) was inserted into the tail vein prior to placing the tumor bearing rat in the magnet. MRS (magnetic resonance spectroscopy) lactate determination and dynamic contrast enhanced magnetic resonance studies were conducted for tumors in the range of 300-2860 mm3 in the Dunning H and 200-2860 in the Dunning R3327AT model. The studies were grouped based on similar tumor volumes for the data analysis. The studies discussed in the previous report which are briefly resummarized since we have more data. For the Dunning R3327-AT tumor, the groups were 110-265 mm^3 (I), 478-649 mm^3 (II), 1035-1207 mm^3 (III), 1409-1708 mm^3 (IV) and 1941-2453 mm^3 (V). For the Dunning H models, the studies were similarly grouped as 227-259 mm^3 (I), 430-546 mm^3 (II), 1000-1236 mm^3 (III), 1382-1715 mm^3 (IV) and 1886-2255 mm^3 (V). Volumes are corrected for 1.3 mm skin thickness. Upon completion of the lactate studies, DCE-MRI (dynamic contrast enhanced magnetic resonance imaging) studies were performed on the rats without removing them from the magnet. Tumor bearing rats were typically studied at 2-5 volumes. After the last study, the tumor bearing rats were injected with pimonidazole (60mg/kg) and excised 60 minutes later. Pimonidazole and H&E staining were performed on tumor slices of 8 micron thickness. Some rats were specifically studied at smaller volumes for comparison to the MR data; in the latter category, the study was terminated at smaller tumor volumes to obtain the histology data.

MR experiments: Magnetic resonance experiments (MRS) Experiments were performed on a Bruker 4.7 T, 40 cm bore animal scanner. A home-made 2 turn volume copper foil coil with a 25 mm diameter was used as a transmit-receive radiofrequency coil for all studies. Scout images were obtained in the three orthogonal directions to ensure that the tumor was positioned within the field of view. MRS lactate detection was performed using the selective multiple quantum coherence (Sel-MQC) (1) sequence, using selective 15 ms single-lobe Sinc pulses. The Sel-MQC sequence selectively detects lactate by selecting the zero quantum (ZQ) → double quantum (DQ) coherence transfer pathway. Phase cycling gradient combinations of g1:g2:g3 = 0:-1:2 with duration $\delta_1 = \delta_2 = 2$ ms, $\delta_3 = 4$ ms, and amplitude of 24 G/cm are used. The pulse sequence parameters for the lactate editing experiments included 512 data points, 8 averages, TR=2 s and a spectral width of 2500Hz. Two-dimensional chemical shift imaging was performed with a matrix size of 16×16 FOV of 40 mm (2.5 x 2.5 mm in plane resolution) and a 5 mm slice thickness generated by a 1ms three-lobe Sinc pulse. The 2D CSI lactate map was coregistered with T2-weighted images of 5 mm slice thickness from the center of the tumor.

Upon completion of the lactate imaging, DCE-MRI studies were performed. Based on the previous scout images, 3 slices in the sagittal direction were imaged using a gradient echo fast imaging (GEFE) sequence with proton density weighted parameters. The acquisition parameters included 2 mm slice thickness, a gap of 0.2 mm, TR/TE/flip angle = 500/3/30°, 256 x 128

matrix, and 2 excitations per phase encoding step. Subsequently the dynamic images were obtained using the same parameters as above except that the TR was reduced to 50ms and 288 data sets were obtained. Gd-DTPA (0.2 mM/kg) was injected intravenously after the first 5 images of the dynamic train had been acquired and these images were used to measure the precontrast signal intensity under saturation conditions.

Data Processing: DCE-MRI data were analyzed using the two compartment model of Hoffman et al (2) to evaluate the rate constant "k_{ep}" and Ak_{ep} (A = amplitude – one of the parameters from the fitting of the data to the model; k_{ep} = rate constant for transfer of Gd-DTPA from the interstitial compartment to the plasma) and slope (rate of increase of signal/time) using IDL programs written previously for clinical studies.
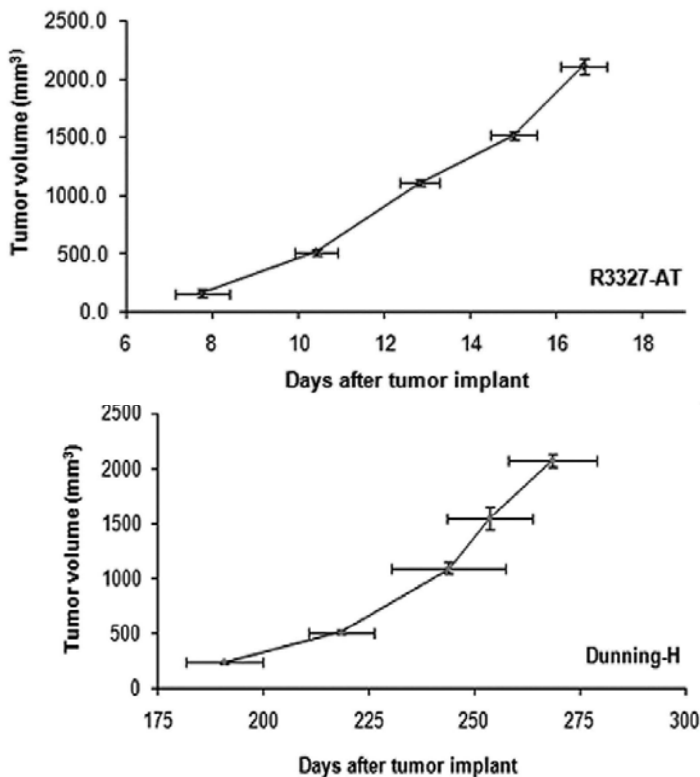
Figure 1a

MRSI: Spatial Fourier transform and superimposition of the spectral grid on the corresponding T2-weighted image were performed using the 3DiCSI software package (courtesy of Truman Brown, Ph.D., Columbia University). The voxels within the tumor were then identified and the free induction decay (FID) from each tumor voxel was extracted. The data for each FID was input to the jMRUI software package and the lactate resonance was fit in the time domain using AMARES (Advanced Method for Accurate, Robust, and Efficient Spectral fitting) (3). The reference phantom 2DCSI set was processed similarly. For quantitation purposes, each tumor voxel was referenced to a phantom voxel at the exact same location. The tumor voxel lactate peak area, the reference voxel lactate peak area, the appropriate T1 saturation factors and the comparative coil loading parameters for tumor and phantom studies and were then used to quantify the tumor voxel lactate.

Figure 1. Tumor volume (mean ± SEM) measurements of Dunning R3327 AT (A) and Dunning H (B) tumors. Note different time scales

D. Results

In last year's report we displayed growth curves for the Dunning R3327AT and Dunning H tumors, preliminary CSI spectra for Dunning R3327AT and H tumors (volume range from about 300 mm3 to 3000mm3), and dynamic contrast enhanced MRI data on the same tumors. We

have by now completed the final analysis and submitted the data (Appendix 2). We summarize the results below (which are taken from Appendix 2).
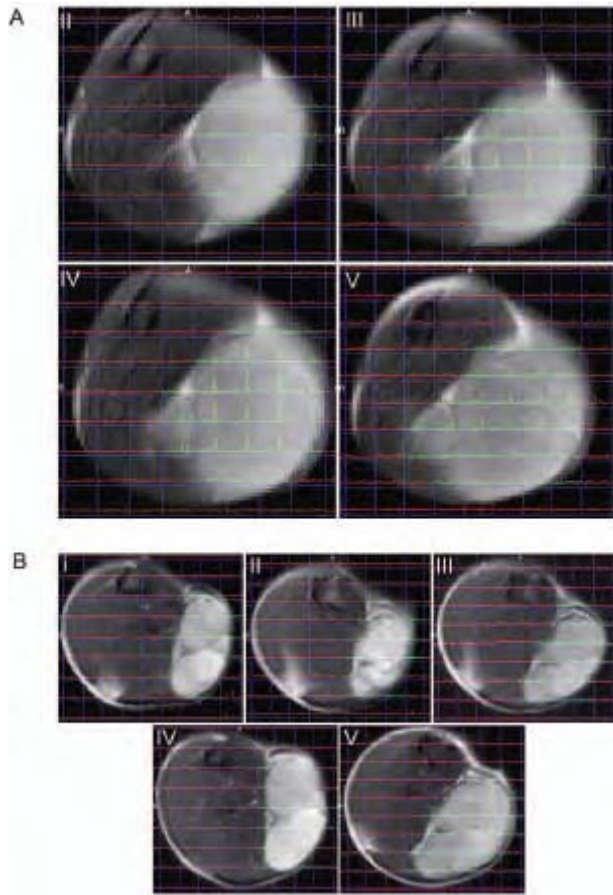

Figure 2A. 2DCSI lactate spectra of R3327 AT prostate tumor model as a function of tumor volume, I:613 mm³, II:1054 mm³, III:1455 mm³ and IV: 2207 mm³. T2 weighted saggital MR tumor image is co-registered with 2DCSI lactate spectra. The peak intensity of the lactate resonance is heterogenous, even within a specific tumor. Figure 2B. 2DCSI lactate spectra of Dunning H prostate tumor model as a function of tumor volume, A: 246 mm³ B:512 mm³, C:1075 mm³, D:1382 mm³ and E: 2255 mm³. T2 weighted saggital MR tumor image is co-registered with 2DCSI lactate spectra. Note the absence of lactate in any of the voxels

In-vivo lactate measurement

The anaplastic, faster-growing R3327-AT cell line had an in vivo tumor doubling time (TDT) of 3.3 ± 0.17 days. The well-differentiated, slower growing Dunning H had a doubling time of 22.8 ± 1.95 days (Figure 1) ($p<0.001$), compatible with previous studies (4).

Figure 2A shows a series of T2 weighted MR images of 5mm thickness co-registered with 2D-CSI lactate spectra obtained on the Dunning R3327 AT tumor. Lactate peaks in the tumor region are highlighted. Lactate was not detected in R3327-AT tumors studied in the volume range 110-265 mm³ (group I; data not shown). As tumor volumes increased to the range of 478-649 mm³ (group II), the average voxel lactate concentration detected was 1.54 ± 0.54 mM (Fig 3A). In group III (tumor volume 1035-1207 mm³), the lactate concentration increased to 4.79 ± 1.67 mM. In Groups IV (1409-1708 mm³) and V (1941-2453 mm³), lactate was 4.64 ± 1.26 mM and 2.71 ± 0.93 mM respectively (Fig 3A, Table 1). The variation of average lactate concentration with growth is shown graphically in Figure 3A and demonstrates the initial increase and subsequent decrease in lactate noted with tumor growth. Results of the non-linear mixed effects analysis showed very significant curvature in the relationship between lactate and tumor volume

($p=0.008$) namely, an initial increase followed by a decrease after reaching a peak that varied among rats at volumes of $1048 +/- 467$ (SD) mm³. There was a significant quadratic or peak effect in the relationship between lactate per voxel and tumor volume ($p<0.001$) in the R3327-AT tumor with significant variation among rats in the volume at which the maximum expected value of (log) lactate occurred.
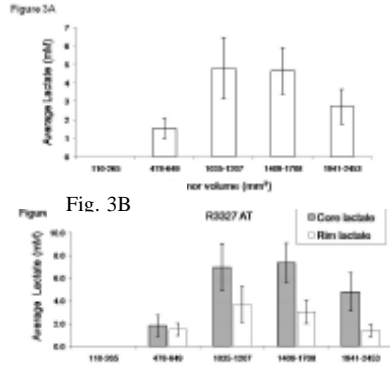
Figure 3A. Measurement of average lactate in R3327 AT tumor model as a function of tumor volume. Tumors in the volume range of 110- 265 mm^3 did not show lactate. Figure 3B. Evaluation of tumor core/rim lactate of R3327 AT tumor model as function of tumor model (solid filled bar plots= core lactate; empty bar plots= rim lactate). Lactate initially increases, shows a plateau, and then decreases in the whole tumor, rim, and core

When the lactate concentration in the outer voxels of the tumor ("rim") was compared to all the other voxels ("core") (Fig. 3B), lactate was significantly higher in the core compared to the rim, independent of tumor volume (p<0.001). The lactate concentration vs tumor volume curve for the core, rim and whole tumor increases to a maximum followed by a decrease after reaching a peak or plateau in groups III and IV. This was characterized by a quadratic term in the statistical model, with a coefficent that was significantly less than zero, reflecting a downturn in lactate concentration with volume after a peak. Inclusion of an additional parameter in the statistical model indicated weak evidence (p=0.09) that on average, the lactate maximum concentration occurred at larger tumor volumes for the core voxels compared to the rim.

A representative set of 2DCSI spectra of Dunning H prostate model at different volumes is represented in Figure 2B (groups I to V). Lactate was not detected in any tumor, regardless of the volume.

DCE-MRI analysis

Dunning R3327-AT
The average Akep for group I tumors was 1.59 ± 0.53 /min. With an increase in tumor size (478 - 649 mm^3), Akep decreased to 0.65 ± 0.12. With further increases in tumor size, the Akep value for group III and IV tumors were 0.55 ± 0.11 and 0.36 ± 0.04 respectively. The largest tumors (group V) had a value of Akep of 0.34 ± 0.05 (Fig. 4A; Table 2A).
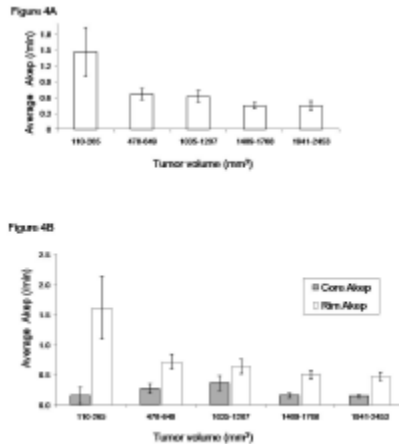
Figure 4A. Whole tumor average Akep (/min) of Dunning R3327 AT tumor model as a function of tumor volume. Akep decreases with tumor volume. Fig 4B. Evaluation of tumor core/rim Akep (/min) of Dunning R3327 AT tumor model at different tumor volumes.

We analyzed whether the rim and core Akep measurements differed. The same criterion for classifying the rim and core voxel was adopted as was used in the lactate analysis (Fig. 4B). The average tumor rim and core Akep value of the lowest tumor volume cohort were 1.61 ± 0.52 /min vs. and 0.15 ± 0.14 /min respectively, but only one of the 4 animals had a tumor large enough to delineate core voxels so the biological significance of this difference is unclear. With the increase in tumor volume to 478-649 mm^3, the tumor rim and core Akep values were 0.71 ± 0.12 /min vs. 0.27 ± 0.07 /min. As expected, there are a greater number of voxels in the rim than in the core. At higher tumor volumes (1035-1207 mm^3 and 1409-1708 mm^3), the rim and core Akep values decreased to 0.63 ± 0.12 /min vs 0.36 ± 0.12 /min and 0.50 ± 0.07 /min

vs 0.15 ± 0.03 /min respectively. At the largest tumor volumes the rim and core Akep values were $0.47 \pm .07$/min and 0.14 ± 0.02/min respectively. The rim Akep values were significantly higher than core values for the Dunning R3327-AT tumors (p<0.001)
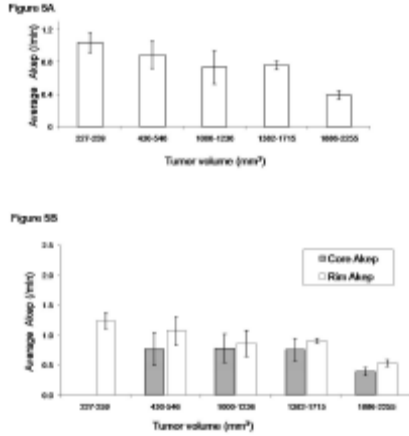
DH tumors

Figure 5A. Whole tumor average Akep (/min) of Dunning H tumor as a function of tumor volume. Figure 5B. Evaluation of tumor core/rim Akep (/min) of Dunning H tumor model over the volume range studied.

Slow growing Group I Dunning H tumor had an average Akep value of 1.23 ± 0.12/min (Fig. 5A, Table 2B). This decreased to 1.06 ± 0.23/min, 0.84 ± 0.21/min and 0.86 ± 0.08/min in groups II, III and IV tumors respectively. With continued tumor growth, the whole tumor Akep values decreased (Group V = 0.46 ± 0.04/min). We subsequently subdivided the analysis to study the rim and core as we had done previously for the Dunning R3327-AT tumor except in the Group I tumors wherein there were no core voxels because of the small tumor size. The rim and core Ak_{ep} values both decreased with growth (p<0.001).

The Dunning H exhibited heterogenous perfusion as manifested by significant differences in Akep value between the rim and core (p<0.023). The Dunning H tumors had significantly higher Akep values than the R3327-AT tumors, as measured in the whole tumor (p<0.001), the core (p<0.001) and the rim (p<0.001). Akep declined progressively over the range of tumor sizes in the Dunning H tumors (p<0.001), particularly at the largest tumor volumes. After applying an appropriate normalizing transformation to Akep (e.g., cube root), the rate of decrease was linear. This decrease was also noted if the data were analyzed separately for the rim and core (p<0.001).

Histology and Immunohistochemistry Correlation

The Dunning R3327-AT tumors have necrosis present even at small tumor volumes (Fig. 6a, b, Fig. 7A). In contrast, the Dunning H tumors had no observable necrosis even at volumes approaching 2300 mm^3, (Figure 6c). In the R33327-AT tumor, we found that with increasing tumor volume, the necrotic fraction increased significantly ($R^2 = 0.808$; p <0.001) (Fig, 7A). A linear correlation between the concentration of lactate measured and the viable tumor volume was noted indicating that the concentration of lactate increases with tumor growth corrected for viability ($R^2 = 0.764$; p=0.005). (Figure 7B)

Tumor sections sequential to those used for histological staining were assessed for the distribution of the hypoxia tracer pimonidazole by immunofluorescence staining (Fig. 6(d), (e), (f)). We observed that the fractional pimonidazole-positive tumor area increased with tumor volume ($R^2 = 0.720$, p = 0.007). Comparison of pimonidazole-positive tumor fraction to lactate values also showed a statistically significant positive correlation ($R^2 = 0.602$, p = 0.023; Fig. 7C).
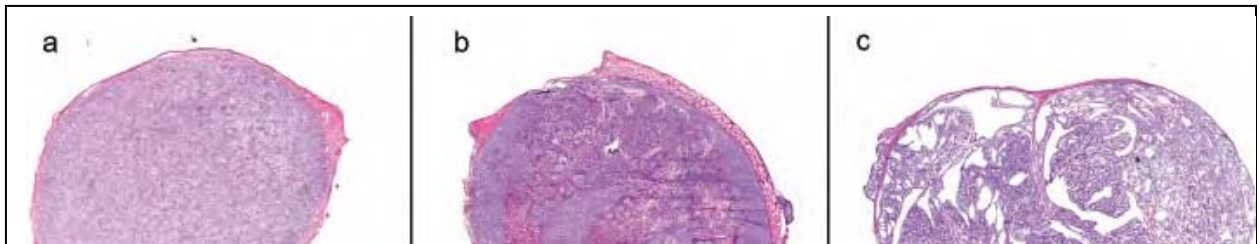
SS-Sel-MQC (Spectral Selective MQC)

In the previous report, we discussed a novel modification of the SelMQC sequence using binomial spectral-selective pulses (SS-SelMQC). Frequency selective excitation pulses were employed with suitable phase cycling of a binomial sequence $\left[(\pi/4)_{\phi_1}-\Delta-(\pi/4)_{\phi_2}\right]$ to selectively excite either lactate methyl CH_3 resonances (ϕ_1, ϕ_2=x, -x) or methylene CH resonances (ϕ_1, ϕ_2=x, x). Frequency selective inversion was achieved using $\left[(\pi/2)_x-\Delta-(\pi/2)_{-x}\right]$ for the lactate methyl CH_3 resonances. Chemical shift selection was achieved by adjusting the interpulse delay equal to the inverse of twice the difference in the center frequencies of maximum and null excitation bands (Fig. 9). In a lipid enriched environment, the modified pulse sequence yielded enhanced lactate signal of 200-300% compared to SelMQC. Non-localized proton spectra and 2D CSI-lactate images were obtained from 30mM lactate/lipid phantoms and *in-vivo* R3327 prostate animal tumors. We concluded that lactate signals detected by SS-SelMQC have a 2-3 times higher signal to noise compared to conventional SelMQC. The sequence is currently being implemented for lactate detection from a volume of interest, which will be used to image the internal organs of transgenic animal tumor models. We have explored this sequence further in the recent year to try to explain the increased signal to noise.
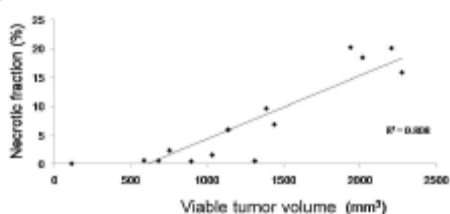
Figure 7A. A graph of percentage of necrosis as a function of tumor volume demonstrates a significant linear correlation between these two parameters.
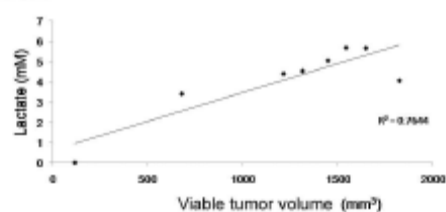
Figure 7B. A graph of the variation of tumor lactate vs. viable tumor volume demonstrating a significant linear correlation. Lactate is noted to increase with tumor growth, when corrected by eliminating the necrotic tissue
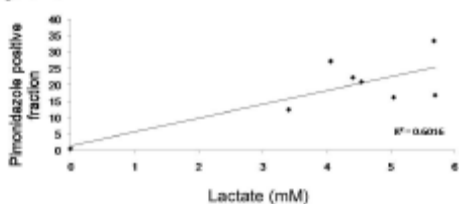
Figure 7C. Graph of pimonidazole positive fraction as a function of measured lactate showing a linear correlation between pimonidazole and lactate concentration. The data suggest that lactate is a potential surrogate for measuring tumor hypoxia in this model.

Table 1 Average lactate concentration and numbers of CSI voxels in the Dunning R-3327-AT tumor

Tumor Group	Tumor volume (mm^3)	Whole tumor		Core		Rim	
		Lactate (mM/L)	Avg # voxels	Lactate (mM/L)	Avg # voxels	Lactate (mM/L)	Avg # voxels
I	110-265	0	7	0	1	0	6
II	478-649	1.53	13	1.79	3	1.46	10
III	1035-1207	4.78	17	6.95	6	3.68	11
IV	1409-1708	4.64	20	7.34	8	3.02	12
V	1941-2453	2.71	24	4.78	10	1.40	14

Average Akep values of Dunning R 3327 AT tumor							Table 2A
Tumor volume (mm^3)	Tumor group	Whole tumor Akep	Rim Akep	Average No. of rim CSI voxels	Core Akep	Average no. of core CSI voxels	
110-265	I	1.59±0.53	1.61±0.52	6	0.15±0.14	1	
478-649	II	0.65±0.12	0.71±0.12	10	0.27±0.07	3	
1035-1207	III	0.55±0.11	0.63±0.12	11	0.36±0.12	6	
1409-1708	IV	0.36±0.04	0.50±0.07	12	0.15±0.03	8	
1941-2453	V	0.34±0.05	0.47±0.07	14	0.14±0.02	10	

Table 2B

Average Akep values of Dunning H tumors						
Tumor volume (mm^3)	Tumor group	Whole tumor Akep	Rim Akep	Average no. of Rim CSI voxels	Core Akep	Average no. of Core CSI voxels
227-259	I	1.23±0.12	1.23±0.12	7	--	0
430-546	II	1.06±0.23	1.07±0.23	9	0.76±0.27	1
1000-1236	III	0.84±0.21	0.85±0.21	11	0.77±0.23	3
1382-1715	IV	0.86±.08	0.90±0.04	13	0.75±0.19	7
1886-2255	V	0.46±.04	0.53±0.05	12	0.38±.06	11

SS-Sel-MQC (Spectral Selective MQC)

In the previous report, we discussed a novel modification of the SelMQC sequence using binomial spectral-selective pulses (SS-SelMQC) (5). Frequency selective excitation pulses were employed with suitable phase cycling of a binomial sequence $\left[(\pi/4)_{\phi_1} - \Delta - (\pi/4)_{\phi_2}\right]$ to selectively excite either lactate methyl CH_3 resonances (ϕ_1, ϕ_2=x, -x) or methylene CH resonances (ϕ_1, ϕ_2=x, x). Frequency selective inversion was achieved using $\left[(\pi/2)_x - \Delta - (\pi/2)_{-x}\right]$ for the lactate methyl CH_3 resonances. Chemical shift selection was achieved by adjusting the interpulse delay equal to the inverse of twice the difference in the center frequencies of maximum and null excitation bands (Fig. 9). In a lipid enriched environment, the modified pulse sequence yielded enhanced lactate signal of 200-300% compared to SelMQC.   Non-localized proton spectra and 2D CSI-lactate images were obtained from 30mM lactate/lipid phantoms and *in-vivo* R3327 prostate animal tumors. We concluded that lactate signals detected by SS-SelMQC have a 2-3 times higher signal to noise compared to conventional SelMQC. The sequence is currently being implemented for lactate detection from a volume of interest, which will be used to image the internal organs of transgenic animal tumor models. We have explored this sequence further in the recent year to try to explain the increased signal to noise.

Reasons for Signal enhancement in SS-SelMQC
Reduced effects of J-scalar coupling evolution, molecular diffusion as well as T_2 relaxation loss in SS-SelMQC are the likely causes of the signal enhancement observed experimentally, compared to SelMQC. These effects were simulated using computer simulations of un-localized lactate signals assuming an *IS* spin system. Lac editing efficiency in SelMQC sequence depends on frequency selective excitation or inversion profiles which necessitates the use of long pulses which increased the MQ evolution period and affects the lactate editing efficiency (1).   In SS-SelMQC, we replaced all the long frequency-selective pulses with short binomial composite RF pulses for frequency selection resulted in shorter MQ evolution delays. This effect increased the Lac editing efficiency by reducing J-coupling evolution as well as molecular diffusion effects as described below.

Scalar coupling effects
Approximately 24 % of the increase in the lactate signal observed in SS-SelMQC (Fig.8A), in comparison with SelMQC (Fig. 8B) (assuming no RF pulse imperfections), can be explained from increased scalar coupling evolution during RF pulse finite widths. We denoted RF pulse imperfection (W_1/W_1^0), where W_1 *and* W_1^0 are actual and ideal RF field strength experienced by samples within RF coils. Hence (W_1/W_1^0) = 1 corresponds to no RF pulse imperfections and (W_1/W_1^0) = 0.9, 0.8 corresponds to the presence of 10% and 20% RF pulse imperfections respectively. In Fig.8A and Fig.8B, the x-axis is the chemical shift scale where the lactate doublet centered on the experimental frequency of CH_3 was plotted without (J≠0) and with (J=0) scalar coupling evolution considered during RF finite pulse widths in the presence of RF pulse imperfections. The y-axis denotes the Fourier transform of total transverse magnetization 'M_{xy}' following the SS-SelMQC and SelMQC sequences. Lac signal intensity was normalized as 100% when there were no scalar coupling effects and RF imperfections. Introducing scalar evolution during finite pulse widths, Lac signal intensity drops to 99% in SS-SelMQC, further
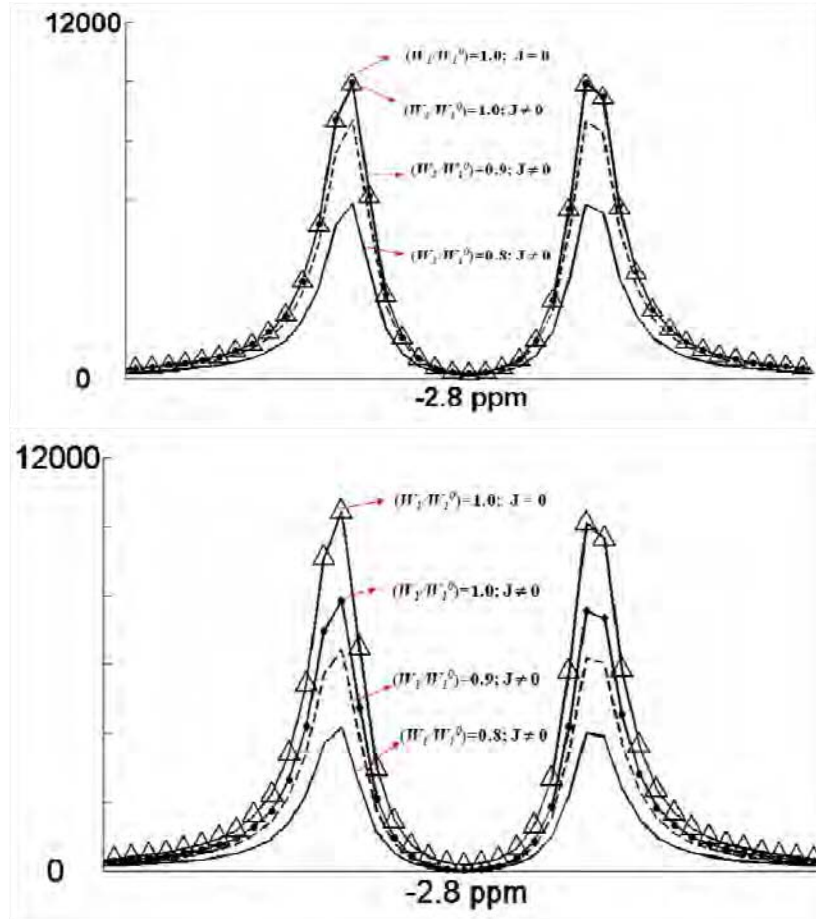
FIG. 8. Computer simulated lactate spectra generated as a function of RF pulse imperfections and scalar coupling evolutions (J _ 0) during RF pulses using **(a)** SS-SelMQC and **(b)** SelMQC sequence. Parameters used for generating these line plots are marked on the figures. Y-axis represents percentage lactate signal normalized to 100% when there were no scalar coupling effects (J _ 0) or RF imperfections. These graphs show simulated spectra of lactate CH3 resonance corresponding to the 4.7T experimental conditions and assuming IS spin system for lactate (CH =I and CH3= S) with scalar coupling JIS _ 7 Hz

reduces to 87% with 10% and 59% with 20% RF pulse imperfections. Similarly, in SelMQC, Lac signal intensity drops to 75%, further reduces to 62% with 10% and 40% with 20% RF pulse imperfections. We can further minimize signal loss observed in simulations due to RF imperfections by customized RF coils generating homogeneous RF fields does this belong here. These simulations yielded a 21 % signal gain for SS-SelMQC compared with SS-SelMQC. It should be noted that for patient studies at the clinical magnetic field strengths of 1.5T or 3.0T, the signal loss due to scalar coupling effects will be more severe using SelMQC compared to SS-SelMQC. The reason for this is that frequency selective pulses used in SelMQC need to be very long as chemical shift dispersion is very low and results in longer t1 MQ evolution delays leading to higher signal loss. Relatively much shorter T1 values can be maintained by binomial selective pulses in SS-SelMQC sequence resulting in minimum scalar coupling losses increases Lac signal sensitivity.

T2 Relaxation Losses

Relatively short T_2 values of lactate have been reported in in-vivo, for eg., rat C6-glioma with 200ms (6) and mice tumors (7) with MCa (68 ms) and Colon-38 tumors (117ms), which would lead to lower Lac detection efficiency. Since the in vivo T_2 relaxation times are short, an optimal sequence minimizing T_2 losses is critical for accurate measurements and for absolute quantification of tissue lactate concentrations. This effect may be particularly important in studies with small tumor volumes, where lactate concentrations may be low, or if used for early cancer diagnosis. Since the total duration of RF pulses in the modified sequence are shorter and approximately 45 ms less than SelMQC sequence, this enhances the lactate signal by 20% (assuming T2=200ms) in the SS-SelMQC method by further reducing T2 relaxation losses.

Molecular Diffusion Effects

When two gradients were applied during MQ evolution period to choose ZQ$\rightarrow$ DQ pathways, Lac signal attenuation occurs due to molecular diffusion of molecules during the period (28) between these gradients of duration δ ms, following the Stejskal-Tanner equation (35). We assumed phantom conditions in our calculations using the diffusion coefficient D= 1 x 10^{-5} cm^2 s^{-1} at room temperature. Using the equation reported earlier (1), the signal loss due to molecular diffusion is as follows,

$$S / S(0) = \exp[-D\{ p(2/\pi\gamma\delta g)\}^2 (\Delta - \tfrac{1}{4}\delta)$$

Where $\Delta = t_1 + \delta + de$, p is the coherence order, de is gradient dead time, γ is gyromagnetic ratio=2.675e8 s^{-1}T$^{-1;}$ for our present SelMQC parameters, the lactate signal loss will be 30 % and signal loss in SS-SelMQC will be only 6 %. Hence a signal gain of 24 % was obtained in SS-SelMQC. The molecular diffusion losses will be severe in choosing DQ$\rightarrow$ZQ pathway to obtain full signal intensity of lactate or at low magnetic field strengths where long pulses result in higher signal loss.

Anti-Angiogenesis Therapy and Predicting Response (Works in Progress).

We are in the process of performing this study where we are evaluating a novel anti-angiogenic drug (RO0281501) and this represents Work in Progress. The tumor bearing rats were divided into two cohorts with similar volumes (treated= 940 mm^3 vs. control =1031 mm^3

respectively). After 24hr of treatment, there was an 18 % tumor growth inhibition (compared to control) and 40 % by day 7 (compared to the control group). Control tumors continued to grow beyond day 7 and became necrotic before day 14, hence these tumor bearing animals were sacrificed. The tumor doubling time (TDT) for the control group was 3.3 +/-0.17 days, whereas the TDT increased to approximately 7-8 days in the treated cohort.
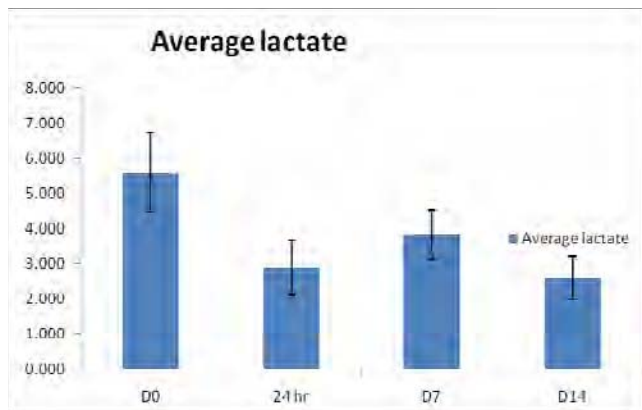
Two dimensional chemical shift imaging (2DCSI) lactate spectra were also obtained at prior to treatment (day 0) and post (24 hr, day 7 and day 14) treatment. Lactate was detected prior to treatment (day 0; 5.6 +/- 1.13 mM/L(mean +/-SEM)) and is significantly ($p < 0.005$) decreased at 24 hrs of treatment (Fig. 9 (2.9 +/- 0.78). At 24 hr post treatment, lactate has poor signal to noise (SNR) (Fig. 10). By day 7, there was no difference between the lactate values measured compared to day 0. At the highest tumor volume (day 14), the tumor lactate decreased to 2.6 +/- 0.61 ($p < 0.03$) compared to day 0. This represents preliminary data and is ongoing.

KEY RESEARCH ACCOMPLISHMENTS:

1. Differences between slow and fast growing tumors in lactate concentration measured. This has been validated by comparison with histology and pimonidazole measurements suggesting changes in perfusion are the cause of lactate detection in the faster growing tumors as they get larger and also induce hypoxia.

2. Development of new, quantitative and more sensitive pulse sequence for lactate measurements implemented.

3. Use of lactate measurements as an early predictor of tumor response to anti-angiogenic therapy - ongoing

4. Use of dynamic contrast enhanced MRI to predict response to anti-angiogenic therapy - ongoing

REPORTABLE OUTCOMES:

Two abstracts were selected for talks in the previous International Society of Magnetic Resonance in Medicine meeting. One of these has now been accepted as a complete manuscript for Magnetic Resonance in Medicine and is In Press (Thakur et al). The second (Yaligar et al) has been written and submitted.   The third is in the process of completing the data analysis and will be complete in about 30 days.

Manuscripts

Thakur SB, Yaligar J, and Koutcher JA. *In-Vivo* Lactate Signal Enhancement Using Binomial Spectral-Selective pulses in SELective MQ Coherence (SS-SelMQC) Spectroscopy. **Magnetic Resonance in Medicine.** In Press.

Yaligar J, Thakur SB, Carlin, S, Thaler HT, Lupu, ME, Wang Y, Matei CC, Zakian KL and Koutcher JA Lactate Imaging and DCE-MRI as surrogate markers of Prostate Tumor Aggressiveness**. Submitted**

Abstracts

1.   Comparative study of tumor lactate and tumor vasculature in aggressive and indolent prostate cancer animal models by 2D-MR Spectroscopic Imaging and DCE-MRI – Yaligar J, Thakur SB, Lupu, ME, Wang Y, Matei CC, Zakian KL and Koutcher JA. Int Society of Magnetic Resonance in Medicine – 16th Annual Meeting, Toronto, May 2008, Page 369

2.   In-Vivo Lactate Detection Using Selective MQ Coherence Spectroscpy: Signal Enhancement Using Spectral-Selective Binomial RF pulses (SS-SelMQC) - Thakur SB, Yaligar J and Koutcher JA. Int Society of Magnetic Resonance in Medicine – 16th Annual Meeting, Toronto, May 2008,

3.   Preclinical evaluation of anti-angiogenic agent RO281501 on R3327 AT prostate model lactate MRS and DCE-MRI. Yaligar J, Thakur SB, Coman M, Lupu ME, Wang Y, Kolinsky K, Higgins B, Zakian KL, and Koutcher JA. Int Society of Magnetic Resonance in Medicine – 16th Annual Meeting, Toronto, May 2008,

CONCLUSION: We have shown that lactate is present in variable amounts in a very aggressive tumor model (R3327AT) which is known to be radiation resistant. At small tumor volumes, where perfusion was better, lactate was not detected. Conversely, in a better perfused, radiation sensitive tumor model (Dunning H), lactate cannot be detected. These data suggest that lactate might be a marker for radiation sensitivity.

More recently, we have shown that changes in lactate occur in response to successful treatment with an anti-angiogenic therapy which is under development. This occurs within 24 hours of treatment. Further analysis of the data stratifying for location is ongoing.

We have developed a modification to the pulse sequence for detecting lactate which is more sensitive and hope to apply it in future experiments. Our preliminary studies suggest that it is approximately twice as sensitive as Sel-MQC and we are currently evaluating the causes for this enhanced sensitivity.

Future Plans

A major hindrance to this study was that the slow growing tumors (Dunning H and HI) were difficult to grow. Currently the Dunning HI is growing well and is ready for transplanting to a larger cohort of rats. Additionally, the Dunning H was obtained from a second source (Dr. Ralph Mason) and is growing, albeit slowly as expected. We will evaluate these lines for 1) presence of lactate in the HI, 2) response to anti-angiogenic therapy and the utility of DCE-MRI and lactate changes to predict response, and compare the lactate measurements with a PET tracer of hypoxia (18F-fluoromisonidazole) and metabolism (18FDG)to determine if lactate could be considered as a surrogate of hypoxia and if it provides equivalent data to FDG since both are probes of tumor glycolysis. By the use of the new pulse sequence developed by Dr. Thakur, we intend to improve the resolution of the lactate study will be improved to that of the PET study (~2 x 2 x 2 mm). We have had extensive experience doing multi-modality studies using different instruments and registering the data and do not anticipate any problems with image registration (8-10).

REFERENCES:

1. <u>He Q</u>, <u>Shungu DC</u>, <u>van Zijl PC</u>, <u>Bhujwalla ZM</u>, <u>Glickson JD</u>. Single-scan in vivo lactate editing with complete lipid and water suppression by selective multiple-quantum-coherence transfer (Sel-MQC) with application to tumors. <u>J Magn Reson B.</u> 1995 Mar;106(3):203-11

2. Hoffman U, Brix G, Knopp MV et al. Pharmacokinetic mapping of the breast: A new method for dynamic MR mammography. Magn Reson Med33:506-514, 1995

3. Vanhamme L, van den Boogart A, Van Huffel S. Improved method for accurate and efficient quantification of MRS data with use of prior knowledge. J Magn Res 129: 35-43, 1997

4. Thorndyke C, Meeker BE, Thomas G, Lakey WH, McPhee MS, Chapman JD. The radiation sensitivities of R3327-H and R3327-AT rat prostate adenocarcinomas. J Urol 1985; 134:191-8

5. Thakur SB, Yaligar J, Koutcher JA <u>In vivo lactate signal enhancement using binomial spectral-selective pulses in selective MQ coherence (SS-SelMQC) spectroscopy.</u> Magn Reson Med. 2009 Sep;62(3):591-8

6. Terpstra M, High WB, Luo Y, de Graaf RA, Merkle H, Garwood M. Relationships among lactate concentration, blood flow and histopathologic profiles in rat C6 glioma. NMR Biomed 1996;9:185–194.

7. Muruganandham M, Koutcher JA, Pizzorno G, He Q. In vivo tumor lactate relaxation measurements by selective multiple-quantum-coherence (Sel-MQC) transfer. Magn Reson Med 2004;52:902–906

8. Humm JL, Ballon D, Hu J, Ruan S, Chui C, Tulipano PK, Erdi A, Koutcher J, Zakian K, Urano M, Zanzonico P, Mattis C, Dyke J, Chen Y, Harrington P, O'Donoghue JA and Ling CC. A stereotactic method for the three-dimensional registration of multi-modality biologic images in animals: NMR, PET, histology, and autoradiography. J. of Computerized Tomography, 2003 Sep;30(9):2303-14

9. Zhang M, Huang M, Le C, Zanzonico PB, Claus F, Kolbert KS, Martin K, Ling CC, Koutcher JA, Humm JL. Accuracy and reproducibility of tumor position during prolonged and multi-modality animal imaging studies. Physics in Med and Bol. 2008 Sep 30;53(20):5867-5882

10. Cho HJ, Ackerstaff A, Carlin S, Lupu ME, Wang Y, Rizwan A, O'Donoghue J, Ling CC, Humm JL, Zanzonico PB, Koutcher JA. Noninvasive Multimodality Imaging of the Tumor Microenvironment: Registered Dynamic MRI and PET Studies of a Preclinical Tumor Model of Tumor Hypoxia. Neoplasia, 11(3) 247–259, 2009

APPENDICES:

Manuscripts

Thakur SB, Yaligar J, and Koutcher JA. *In-Vivo* Lactate Signal Enhancement Using Binomial Spectral-Selective pulses in SELective MQ Coherence (SS-SelMQC) Spectroscopy. Magnetic Resonance in Medicine. In Press

Yaligar J, Thakur SB, Carlin, S, Thaler HT, Lupu, ME, Wang Y, Matei CC, Zakian KL and Koutcher JA Lactate Imaging and DCE-MRI as surrogate markers of Prostate Tumor Aggressiveness. **Clinical Cancer Research - submitted**

Your article (08-10316) from Magnetic Resonance in Medicine is available for download

_____

Magnetic Resonance in Medicine Published by John Wiley & Sons, Inc.

Dear Author,

Your article page proofs for Magnetic Resonance in Medicine are ready for review. John Wiley & Sons has made this article available to you online for faster, more efficient editing. Please follow the instructions below and you will be able to access a PDF version of your article as well as relevant accompanying paperwork.

First, make sure you have a copy of Adobe Acrobat Reader software to read these files. This is free software and is available for user downloading at http://www.adobe.com/products/acrobat/readstep.html.

Open your web browser, and enter the following web address:
http://rapidproof.cadmus.com/RapidProof/retrieval/index.jsp

You will be prompted to log in, and asked for a password. Your login name will be your email address, and your password will be 88CetsdRc88L

Example:

Login: your e-mail address
Password: 88CetsdRc88L

The site contains one file, containing:

- Author Instructions Checklist
- Adobe Acrobat Users - NOTES tool sheet
- Reprint Order form
- A copy of your page proofs for your article

Print out this file, and fill out the forms by hand. (If you do not wish to order reprints, please mark a "0" on the reprint order form.) Read your page proofs carefully and:

- indicate changes or corrections in the margin of the page proofs
- answer all queries (footnotes A,B,C, etc.) on the last page of the PDF proof
- proofread any tables and equations carefully
- check your figure legends for accuracy

Within 48 hours, please return via fax or express mail all materials to the address given below. This will include:

1) Page proofs with corrections
2) Reprint Order form

Return to:

MRM Production Team
John Wiley & Sons, Inc.
111 River Street, Hoboken, NJ 07030

Email: mrm@wiley.com
Fax: 201-748-6281/6182

Technical problems? If you experience technical problems downloading your file or any other problem with the website listed above, please contact Teressa Beard at beardt@cadmus.com.

Questions regarding your article? Please don't hesitate to contact the MRM Production Team at mrm@wiley.com with any questions about the article itself, or if you have trouble interpreting any of the questions listed at the end of your file. REMEMBER TO INCLUDE YOUR ARTICLE NO. (08-10316) WITH ALL CORRESPONDENCE. This will help both of us address your query most efficiently.

As this e-proofing system was designed to make the publishing process easier for everyone, we welcome any and all feedback. Thanks for participating in our e-proofing system!

This e-proof is to be used only for the purpose of returning corrections to the publisher.

Sincerely,

MRM Production Team
John Wiley & Sons, Inc.
111 River Street, Hoboken, NJ 07030

Email: mrm@wiley.com
Fax: 201-748-6281/6182

WILEY

Publishers Since 1807

111 River Street, Hoboken, NJ 07030

IMMEDIATE RESPONSE REQUIRED

Your article will be published online via Wiley's EarlyView® service (www.interscience.wiley.com) shortly after receipt of corrections. EarlyView® is Wiley's online publication of individual articles in full text HTML and/or pdf format before release of the compiled print issue of the journal. Articles posted online in EarlyView® are peer-reviewed, copyedited, author corrected, and fully citable via the article DOI (for further information, visit www.doi.org). EarlyView® means you benefit from the best of two worlds--fast online availability as well as traditional, issue-based archiving.

Please follow these instructions to avoid delay of publication.

READ PROOFS CAREFULLY

- This will be your <u>only</u> chance to review these proofs. **Please note that once your corrected article is posted online, it is considered legally published, and cannot be removed from the Web site for further corrections.**
- Please note that the volume and page numbers shown on the proofs are for position only.

ANSWER ALL QUERIES ON PROOFS (Queries for you to answer are attached as the last page of your proof.)

- Mark all corrections directly on the proofs. Note that excessive author alterations may ultimately result in delay of publication and extra costs may be charged to you.

CHECK FIGURES AND TABLES CAREFULLY)

- Check size, numbering, and orientation of figures.
- All images in the PDF are downsampled (reduced to lower resolution and file size) to facilitate Internet delivery. These images will appear at higher resolution and sharpness in the printed article.
- Review figure legends to ensure that they are complete.
- Check all tables. Review layout, title, and footnotes.

COMPLETE REPRINT ORDER FORM

- Fill out the attached reprint order form. It is important to return the form <u>even if you are not ordering reprints</u>. You may, if you wish, pay for the reprints with a credit card. Reprints will be mailed only after your article appears in print. This is the most opportune time to order reprints. If you wait until after your article comes off press, the reprints will be considerably more expensive.

RETURN   PROOFS
REPRINT ORDER FORM
CTA (If you have not already signed one)

RETURN IMMEDIATELY AS YOUR ARTICLE WILL BE POSTED ONLINE SHORTLY AFTER RECEIPT;
FAX PROOFS TO (+1) 201-748-6182 or 6281

QUESTIONS?   **MRM Production Team**
                    E-mail: mrm@wiley.com

                    Refer to journal acronym and article production number
                    (i.e., MRM 00-0001or 104-0000).

Softproofing for advanced Adobe Acrobat Users - NOTES tool

NOTE: ACROBAT READER FROM THE INTERNET DOES NOT CONTAIN THE NOTES TOOL USED IN THIS PROCEDURE.

Acrobat annotation tools can be very useful for indicating changes to the PDF proof of your article. By using Acrobat annotation tools, a full digital pathway can be maintained for your page proofs.

The NOTES annotation tool can be used with either Adobe Acrobat 6.0 or Adobe Acrobat 7.0. Other annotation tools are also available in Acrobat 6.0, but this instruction sheet will concentrate on how to use the NOTES tool. Acrobat Reader, the free Internet download software from Adobe, DOES NOT contain the NOTES tool. In order to softproof using the NOTES tool you must have the full software suite Adobe Acrobat Exchange 6.0 or Adobe Acrobat 7.0 installed on your computer.

Steps for Softproofing using Adobe Acrobat NOTES tool:

1. Open the PDF page proof of your article using either Adobe Acrobat Exchange 6.0 or Adobe Acrobat 7.0. Proof your article on-screen or print a copy for markup of changes.

2. Go to Edit/Preferences/Commenting (in Acrobat 6.0) or Edit/Preferences/Commenting (in Acrobat 7.0) check "Always use login name for author name" option. Also, set the font size at 9 or 10 point.

3. When you have decided on the corrections to your article, select the NOTES tool from the Acrobat toolbox (Acrobat 6.0) and click to display note text to be changed, or Comments/Add Note (in Acrobat 7.0).

4. Enter your corrections into the NOTES text box window. Be sure to clearly indicate where the correction is to be placed and what text it will effect. If necessary to avoid confusion, you can use your TEXT SELECTION tool to copy the text to be corrected and paste it into the NOTES text box window. At this point, you can type the corrections directly into the NOTES text box window. **DO NOT correct the text by typing directly on the PDF page.**

5. Go through your entire article using the NOTES tool as described in Step 4.

6. When you have completed the corrections to your article, go to Document/Export Comments (in Acrobat 6.0) or Comments/Export Comments (in Acrobat 7.0). Save your NOTES file to a place on your harddrive where you can easily locate it. **Name your NOTES file with the article number assigned to your article in the original softproofing e-mail message.**

7. **When closing your article PDF be sure NOT to save changes to original file.**

8. To make changes to a NOTES file you have exported, simply re-open the original PDF proof file, go to Document/Import Comments and import the NOTES file you saved. Make changes and reexport NOTES file keeping the same file name.

9. When complete, attach your NOTES file to a reply e-mail message. Be sure to include your name, the date, and the title of the journal your article will be printed in.

C1

WILEY

Publishers Since 1807

REPRINT BILLING DEPARTMENT ∉ 111 RIVER STREET ∉ HOBOKEN, NJ 07030
PHONE: (201) 748-8789; FAX: (201) 748-6326
E-MAIL: reprints@wiley.com
PREPUBLICATION REPRINT ORDER FORM

Please complete this form even if you are not ordering reprints. This form **MUST** be returned with your corrected proofs and original manuscript. Your reprints will be shipped approximately 4 weeks after publication. Reprints ordered after printing will be substantially more expensive.

JOURNAL   **Magnetic Resonance in Medicine** _____ VOLUME _____ ISSUE _____

TITLE OF
MANUSCRIPT _____

MS. NO.   MRM   NO. OF   AUTHOR(S)
                         PAGES

No. of Pages	100 Reprints	200 Reprints	300 Reprints	400 Reprints	500 Reprints
	$	$	$	$	$
1-4	336	501	694	890	1052
5-8	469	703	987	1251	1477
9-12	594	923	1234	1565	1850
13-16	714	1156	1527	1901	2273
17-20	794	1340	1775	2212	2648
21-24	911	1529	2031	2536	3037
25-28	1004	1707	2267	2828	3388
29-32	1108	1894	2515	3135	3755
33-36	1219	2092	2773	3456	4143
37-40	1329	2290	3033	3776	4528

**REPRINTS ARE ONLY AVAILABLE IN LOTS OF 100. IF YOU WISH TO ORDER MORE THAN 500 REPRINTS, PLEASE CONTACT OUR REPRINTS DEPARTMENT AT (201) 748-8789 FOR A PRICE QUOTE.

☐   Please send me _____ reprints of the above article at $ _____

Please add appropriate State and Local Tax   (Tax Exempt No._____) $ _____
for United States orders only.

                                        Please add 5% Postage and Handling $ _____

                    TOTAL AMOUNT OF ORDER** $ _____

**International orders must be paid in currency and drawn on a U.S. bank

Please check one: ☐   Check enclosed   ☐   Bill me   ☐   Credit Card
If credit card order, charge to: ☐   American Express   ☐   Visa   ☐   MasterCard

Credit Card No _____   Signature _____   Exp. Date _____

BILL TO: **SHIP TO:**   (Please, no P.O. Box numbers)
Name _____   Name _____

Institution _____   Institution _____

Address _____   Address _____

_____   _____

Purchase Order No. _____   Phone _____   Fax _____

                                                    E-mail _____

WILEY
Publishers Since 1807

COLOR REPRODUCTION IN YOUR ARTICLE

These proofs have been typeset using the original figure files transmitted to production when this article was accepted for publication. Please review and mark your approval of each figure individually within your proof corrections. Should you need further assistance, please contact Kim Bernard by e-mail **kbernard@wiley.com**.

Because of the high cost of color printing we can only print figures in color if authors cover the expense. If you have submitted color figures please indicate your consent to cover the cost on the table listed below by marking the box corresponding to the approved cost on the table. The journal offers one page of color free of charge, the cost for subsequent color pages is $500 USD per printed page regardless of the number of figures appearing on the page.

Please note, all color images will be reproduced online at no charge, whether or not you opt for color printing.

You will be invoiced for color charges once the article has been published in print.

Failure to return this form with your article proofs will delay the publication of your article.

JOURNAL   **MRM** _____   MS. NO. _____   NO. COLOR PAGES _____

MANUSCRIPT TITLE   _____

AUTHOR(S)   _____

No. Color Pages	Color Charge	No. Color Pages	Color Charge	No. Color Pages	Color Charge
☐ 1	$0	☐ 5	$2000	☐ 9	$4000
☐ 2	$500	☐ 6	$2500	☐ 10	$4500
☐ 3	$1000	☐ 7	$3000	☐ 11	$5000
☐ 4	$1500	☐ 8	$3500	☐ 12	$5500
Contact kbernard@wiley.com for a quote if you have more than 12 pages of color					

☐ Please print my figures color   ☐ Please print my figures in black and white

☐ Please print the following figures in color   _____

and convert these figures to black and white   _____

Approved by   _____

Billing Address   _____   E-mail   _____

_____   Telephone   _____

_____   Fax   _____

In Vivo Lactate Signal Enhancement Using Binomial Spectral-Selective Pulses in Selective MQ Coherence (SS-SelMQC) Spectroscopy

S.B. Thakur,[1,2]* J. Yaligar,[1] and J.A. Koutcher[1–3]

Tumor vasculature and tissue oxygen pressure can influence tumor growth, metastases, and patient survival. Elevated levels of lactate may be observed during the process of aggressive tumor development accompanied by angiogenesis (the evolution of the microenvironment). The noninvasive MR detection of lactate in tumor tissues as a potential biomarker is difficult due to the presence of co-resonating lipids that are present at high concentrations. Methods were previously reported for lactate editing using the SELective Multiple Quantum Coherence (SelMQC) method. Here we report a sequence "SS-SelMQC," Spectral-Selective SelMQC, which is a modified version of SelMQC using binomial pulses. Binomial pulses were employed in this editing sequence for frequency excitation or inversion of selective lactate resonances. Lactate detection has been demonstrated using SS-SelMQC, both in vitro (30 mM lactate/H_2O doped with 25 μM Gd-DTPA) and in vivo (Dunning R3337-AT prostate tumors), and compared to similar measurements made with SelMQC. Lactate areas were measured from nonlocalized spectra, one-dimensional (1D) localized spectra, and two-dimensional chemical shift images (CSI) of the localized slice. In data from whole phantoms, the modified pulse sequence yielded enhancement of the lactate signal of 2.4 ± 0.40 times compared to SelMQC. Similar in vivo lactate signal enhancement of 2.3 ± 0.24 times was observed in 1D slice-localized experiment.   Magn Reson Med 62:000–000, 2009. © 2009 Wiley-Liss, Inc.

Key words: lactate editing; single-scan lipid suppression; spectral-selective binomial pulses; 2D chemical shift imaging

In vivo proton MR spectroscopy (MRS) provides a noninvasive, biochemical measure of metabolism which can be used to differentiate healthy tissues from tumor tissues based on the metabolic abnormalities (1–3). Metabolites may be a priori markers of prognosis or metabolic changes can be very sensitive early indicators of treatment response. As such, metabolic approaches show promise for monitoring, and perhaps ultimately selecting treatments. As tumors are heterogeneous, multivoxel MRS imaging (MRSI) provides a method to investigate therapy response and optimization of individual treatment regime based on various metabolite levels or concentrations within each voxel, which might signify aggressive (or indolent) disease (4–8) in local regions of the tumor. Among the many detectable metabolites, lactate (Lac) is an important compound that reflects elevated tumor glycolysis and/or poor tissue perfusion, which may result in accelerated tumor growth, malignant transformation, and metastases (9). Lac is the endproduct of glycolysis and the methyl resonance peak is typically a doublet situated at 1.3 ppm. Different levels of tumor lactate in the MR spectrum were reported in the literature (10–15). High Lac was observed in extracts from biopsy specimens of breast tumors (10,16) and prostate tumors (11). Low extracellular pH and high Lac levels were shown to be indicators of metastatic risk in breast cancer xenografts (12,13). Elevated Lac content in biopsy samples was shown to correlate with increased risk of metastasis and poor patient survival in head and neck cancer (14) and cervical cancer (15), while a decrease in steady-state tumor Lac levels related to tumor response to radiation (17,18) and chemotherapy (19,20). It has also been shown by Pavel et al. (21) that Lac is likely to be found in malignant breast tumors that may be a marker for tumor diagnosis. Therefore, noninvasively measured Lac may be an additional characteristic metabolic marker for cancer studies and may improve diagnostic specificity, serve as an early marker of tumor response, and provide functional information about prognosis.

AQ: 1

Reliable measurement and interpretation of MRS-derived metabolites requires knowledge of the factors affecting Lac resonance detection and quantitation. Detection of relatively low Lac levels in tumor tissues using conventional MRS techniques such as PRESS (22) and STEAM (23) is a challenging task due to the presence of the intense co-resonant lipid (Lip) signals. To differentiate Lac from the co-resonating Lip resonances, spectral editing techniques, such as spin-echo (SE) J-difference spectroscopy (24) and multiple-quantum (MQ) coherence filters (25–28), have frequently been employed. Although the J-difference approach detects lactate with 100% signal sensitivity, the subtraction of sequential scans with different echo times (TE) for lipid suppression can cause artifacts resulting from subject motion and instrumental instabilities. MQ filters alleviate the problem of motion artifacts by the technique of a single-shot acquisition. However, these sequences generally exhibit signal contamination from residual lipid MQ coherences (25,26). In contrast, the selective MQ-coherence (SelMQC) transfer sequence avoids excitation of lipid MQ coherences, and thus offers complete

---

[1]Department of Medical Physics, Memorial Sloan Kettering Cancer Center, New York, New York.

[2]Department of Radiology, Memorial Sloan Kettering Cancer Center, New York, New York.

[3]Department of Medicine, Memorial Sloan Kettering Cancer Center, New York, New York.

*Correspondence to: Dr. Sunitha B. Thakur, Department of Medical Physics and Radiology, Memorial Sloan Kettering Cancer Center, 1275 York Ave., New York, NY 10065. E-mail: thakurs@mskcc.org
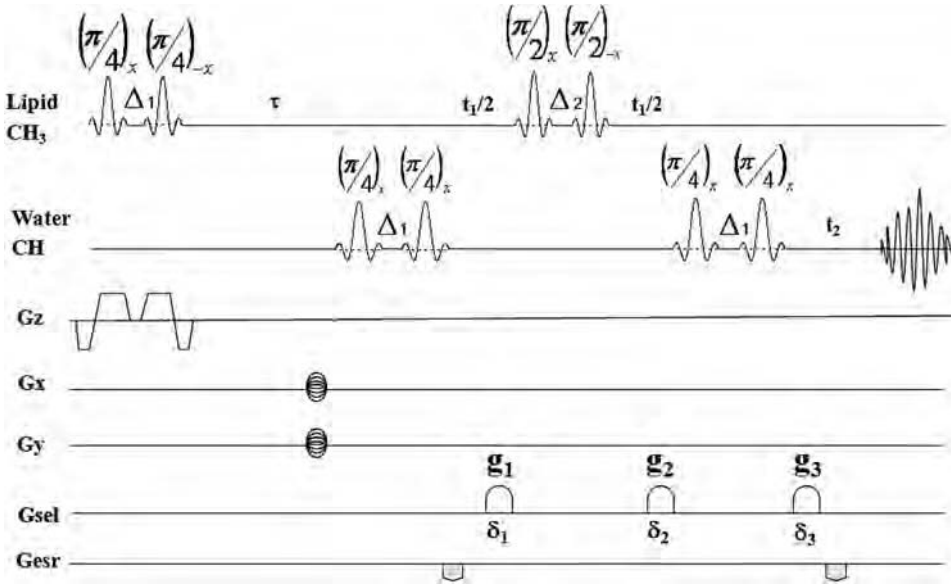
Thakur et al.

FIG. 1. The SS-SelMQC pulse sequence. The ZQ→DQ coherence transfer pathway is selected with the G_{sel} gradients in a ratio of g_1: g_2: g_3 = 0: −1: 2 (0: −14 G/cm: 28 G/cm) with duration $\delta_1 = \delta_2 = \delta_3 = 2$ ms. All other parameters are given in Materials and Methods.

lipid and water suppression in a single scan (28). Like most other MQ filters, the SelMQC sequence has the disadvantage of recovering only 50% of the lactate signal, due to the selection of a single coherence-transfer pathway. Although full Lac signal recovery is possible, a two-step phase cycling procedure is required to refocus the lipid single quantum coherences and makes this method susceptible to motion artifacts. The conversion of this edited signal into accurate tissue concentrations of Lac requires corrections for signal loss arising from various additional sources. These include molecular diffusion, scalar coupling (J) effects, RF pulse imperfections, spin-lattice (T_1), and spin-spin (T_2) relaxation times.

In previous work (28), the SelMQC technique has been developed for selective detection of Lac CH_3 protons without any interference from water and co-resonating lipid resonances. This technique has been successfully applied for lactate detection in breast cancer (21), the detection of an antineoplastic agent Iproplatin in murine RIF-1 tumors (27), and for detecting early response to cyclophosphamide treatment of RIF-1 tumors (17). Although this sequence's efficiency for Lac editing with Lip suppression depends on selective excitation with RF pulses, it was shown that substituting a slice selective pulse for the first frequency selective RF pulse results in tolerable residual lipid resonances (28). To ensure complete lipid suppression, two-step phase cycling of the first CH pulse with respect to the receiver is needed, which again may have motional instabilities.

Here we report a novel modification of the SelMQC, spectral-selective SelMQC (SS-SelMQC) sequence (Fig. 1) using composite binomial pulses (29) for Lac detection in nonlocalized and slice-localization versions, with complete removal of lipid and water resonances. Lactate spectra from nonlocalized, one-dimensional (1D) localized sagittal slice and two-dimensional (2D) CSI-lactate images were obtained from 30 mM Lac/Lip phantoms and in vivo Dunning R3327 prostate animal tumors using our sequence and compared with the SelMQC sequence. Theoretical simulations were generated to understand the performance of the new sequence for different parameters employed in our experiments.

MATERIALS AND METHODS

Theoretical

In the literature (30), composite binomial pulses with increasing order were described as {1-1}, {1-2-1}, {1-3-3-1}, etc. Initially binomial pulses were designed for spectral-selective excitation or inversion of spin resonances with water suppression in NMR spectroscopy (30). In recent years the behavior of these pulses was explored for application to spatial selection in addition to spectral selection, particularly for water-fat MR imaging (31–33). RF pulses and slice select gradients for composite spatial-spectral pulses were applied in different ways (31).

In our present study we used a {1-1} composite pulse consisting of two RF pulses of equal amplitude with spacing (Δ) between them. Frequency selective excitation was achieved by using a binomial pulse block $[(\pi/4)_{\phi_1} - \Delta - (\pi/4)_{\phi_2}]$ and adjusting the phases of RF pulses to selectively excite either off-resonant Lac CH_3 (spin I) resonances (ϕ_1, ϕ_2 = x, −x) or on-resonant CH (spin S) resonances (ϕ_1, ϕ_2 = x, x). Frequency selective inversion was achieved using $[(\pi/2)_x - \Delta - (\pi/2)_{-x}]$ for the Lac CH_3 resonances without perturbing CH chemical shift. The time difference between the pulses, "Δ," is equal to the reciprocal of twice the difference of the center frequencies of maximum (v_I) and null (v_S) excitation bands of I and S resonances,

$$\Delta = \frac{1}{2\delta v_{IS}},$$

where δv_{IS} is the frequency difference I and S resonances.

When RF pulses are considered as delta pulses, Δ is the time delay between two elements of the {1-1} composite pulse. Under our experimental conditions where the RF pulses are shaped pulses with finite pulse widths, Δ needs to be corrected for finite pulse width effects. If we assume $pw_{(\pi/4)}$ and $pw_{(\pi/2)}$ are pulse widths of ($\pi/4$) and ($\pi/2$) RF

pulses within binomial 90° and 180° composite pulses, then Δ_1 ($\Delta - pw_{(\pi/4)}$) and Δ_2 ($\Delta - pw_{(\pi/2)}$) are the effective interpulse delays (pulse width corrected) for 90° and 180° binomial blocks, respectively.

Numerical computer simulations were generated to calculate the selectivity of these pulses for the Lac "IS" spin system using spin density matrix calculations assuming the experimental field strength of 4.7T. The response of a nuclear spin ensemble to multiple RF irradiation pulses often deviates from the expected or the desired effect, primarily due to imperfections such as the spatial inhomogeneity of the RF field and off-resonance effects. Due to the long durations of the shaped RF pulses, evolution due to scalar couplings and chemical shifts of both spins needs to be considered. The Hamiltonian of an IS system during the application of a RF pulse and free evolution (no RF effect) in the doubly rotating frame are given by

$$H_{RF}(t) = \omega_{1I}(t)(I_x\cos\phi(t) + I_y\sin\phi(t))$$
$$+ \omega_{1S}(t)(S_x\cos\phi(t) + S_y\sin\phi(t)) \quad [1]$$

and

$$H = \Delta\omega_I I_z + \Delta\omega_S S_z + 2\pi J_{IS}I_zS_z \quad [2]$$

where $\Delta\omega_I$, $\Delta\omega_S$, J_{IS} are chemical shifts of I, S spins, and scalar coupling. $\omega_{1I}(t)$, $\omega_{1S}(t)$, and $\phi(t)$ are the RF field strengths in 3-lobe sinc shape with step duration "t" on I and S spins, and their phase, respectively. We examined the transient response of this spin system following the SS-SelMQC pulse sequence in the absence of the slice gradient which can be described as:

$$\rho(t_2) = U_{total} \times \rho(0) \times U_{total}^{-1} \quad [3]$$

where $\rho(0)$ represents the equilibrium density matrix and the RF pulse effect was calculated from the Hamiltonian using Eq. [1] by considering the scalar evolution term in addition to RF terms to account for coupling evolution during finite pulse durations. RF pulses within binomial pulse blocks individually are nonselective pulses and achieve spectral selectivity as an effect of composite blocks.

If we consider $R(\theta,\phi)$ as a rotation propagator representing shaped RF pulse of flip angle θ and phase ϕ and U(t) as a free evolution propagator during time period "t," U_{total} can be written as:

$$U_{total} = U(t_2)R\left(\frac{\pi}{4},x\right)U(\Delta_1)R\left(\frac{\pi}{4},x\right)U(t_1/2)R\left(\frac{\pi}{2},-x\right)$$
$$\times U(\Delta_2)R\left(\frac{\pi}{2},x\right)U(t_1/2)R\left(\frac{\pi}{4},x\right)U(\Delta_1)R\left(\frac{\pi}{4},x\right)$$
$$\times U(\tau)R\left(\frac{\pi}{4},-x\right)U(\Delta_1)R\left(\frac{\pi}{4},x\right) \quad [4]$$

where

$$U(t) = e^{-iHt} \text{ and } R(\theta,\phi) = e^{-i\int_0^{pw} H_{RF}(t)dt} \quad [5]$$

Although the propagator only deals with the first two lines of the pulse sequence, the effect of MQ gradients were considered in the simulation by manually selecting the MQ coherence elements in the density matrix to choose the ZQ→DQ pathway.

Hence, from Eq. [3] the final transverse magnetization is calculated as:

$$<M_{xy}(t)> = [<M_x^2(t)> + <M_y^2(t)>]^{1/2}, \quad [6]$$

where the normalized in-phase $\langle M_x(t)\rangle$ and out-of phase $\langle M_y(t)\rangle$ components of the induced signal are given as:

$$<M_x(t)> = Tr[\rho(t_2)I_x]/Tr[I_x^2], \quad [7]$$

$$<M_y(t)> = Tr[\rho(t_2)I_y]/Tr[I_y^2] \quad [8]$$

This time-domain complex signal is Fourier transformed to obtain the lactate spectra to test the performance of resonance offsets, coupling effects, and RF inhomogeneity. We employed the MatLab software (MathWorks, Natick, MA) to develop a home-built pulse program for simulation of spectral-selective behavior, slice profiles, to study the influence of scalar coupling effects, RF finite pulse width effects, RF inhomogeneity effects, and molecular diffusion effects.

Experimental

All MR imaging and spectroscopy experiments were performed on a 4.7T Bruker Biospin spectrometer (40 cm horizontal bore). Animal studies were conducted in compliance with protocols approved by the animal care protocols in Memorial Sloan-Kettering Cancer Center.

Phantom Preparation

A two-compartment cylindrical phantom (25 mm diameter) was prepared with 30 mM lactate/H_2O doped with 25 μM Gd-DPTA and vegetable shortening (Crisco) side by side. This phantom was used to demonstrate the nonlocalized and localized Lac editing with water and lipid suppression (Fig. 3). A second phantom of 10 mM Lac/D_2O was prepared for generation of slice profile (Fig. 4) and checking the experimental signal loss.

Animal Preparation and Tumor Volume Measurements

Frozen Dunning R3327-AT prostate cancer cells syngeneic to rats were thawed and seeded in 75 cm² flasks. Copenhagen rats, supplied by Charles River Laboratories (Wilmington, MA), were implanted with five million cells subcutaneously in the thigh. Tumor growth was evident visually about 10 days after implantation on the thigh region and volume increased to 800 mm³ to 2600 mm³ (not corrected for skin thickness) in an additional 5–8 days. Tumor volume was calculated as V = (π/6) * x * y * z; where x, y, and z are the length, breadth, and depth of the tumor.

MR experiments were performed at a tumor volume of 857 mm³. Each rat was anesthetized using a mixture of isoflurane (1.5–2.5%) and air and placed in the animal holder. The tumor was adjusted to be placed inside a

2-turn home-built coil (25 mm diameter) tuned to 200 MHz and matched to 50 ohms prior to initiating MR experiments. The animal was placed inside a custom-designed MR platform with a 315 mm long section of 120 mm diameter plastic tube (the center of this platform matches with isocenter of the magnet). The animal was positioned in the center of this plastic cradle containing an RF coil and was held in place with tape. Temperature was maintained at 37°C. The magnet was shimmed and resulted in a full width at half maximum peak height (FWHM) of less than 50 Hz for the water resonance in vivo.

MR Imaging

The Bruker ParaVision Tripilot pulse sequence was used to create three perpendicular images (field of view [FOV] = 40 mm) as scout images for positioning of the animal tumor within the coil to ensure that the tumor was in the center of the magnet. Using these Tripilot scout images, T_2-weighted MR sagittal images with a 5 mm thickness, using a multislice multiecho (MSME) sequence (repetition time [TR] = 3734 ms; echo time [TE] = 30 ms; 512×128 matrix, number of excitations [NEX] = 2; FOV = 40 mm) were obtained from the tumor located at isocenter. Total MR image acquisition including shimming took about 10 min.

MR Spectroscopy

Nonlocalized Lac MR spectra from whole phantom/tumors, 1D localized 5 mm sagittal slice, as well as 2D CSI images from a sagittal slice were collected using SS-SelMQC sequence and compared with the previously reported SelMQC sequence (28). In vitro Lac/Lip phantom and in vivo R3327-AT prostate tumors were studied.

The MR spectroscopy acquisition parameters for SelMQC (28) included a 1 ms three-lobe sinc shaped slice-selective pulse and a frequency selective 15 ms single-lobe Sinc RF pulses for frequency selective excitation and inversion of CH and CH_3 resonances. In SS-SelMQC we used a high-power three-lobe sinc shaped RF pulses for both $(\pi/4)$ (200 μs duration) and $(\pi/2)$ (400 μs duration) flip angles, a pulse repetition time (TR) of 2 sec, and spectral width of 2500 Hz; t_1 = 2 ms; Δ_1 = 693 μs; Δ_2 = 493 μs (see Fig. 1). Due to RF finite pulse widths within the binomial pulse blocks, Δ_1 and Δ_2 values were adjusted to include the chemical shift evolution starting from the center of the first pulse to the center of the second pulse. In the binomial spectral-selective pulses we chose to use broadband sinc shaped RF pulses. A slice gradient (trapezoidal shape) was applied to choose a 5 mm or 10 mm slice thickness. Gradient rise time and ramp down times were typically 100–150 μs. A phase cycling gradient scheme with g_1: g_2: g_3 = 0: −1: 2 (0: −14 G/cm: 28 G/cm) with duration $\delta_1 = \delta_2 = \delta_3$ = 2 ms was employed in both sequences for the selection of ZQ→DQ coherence selection pathway. The transmitter was set at the *CH* frequency. The Lac *CH* resonance frequency is at 4.1 ppm compared to the water signal (4.8 ppm). Whole tumor and 1D slice localized Lac spectra were obtained with 16 transients, respectively, without and with the application of slice-selection, and no phase encoding gradients were applied. The 2D ^{1}H CSI data were collected by applying 16×16 phase encoding steps and FOV = 40 mm, which results in a voxel size of $2.5 \times 2.5 \times 5$ mm^3. The total time for the 2D CSI experiment was ≈1 hr 15 min (NEX = 8). The anatomical sagittal T_2-^{1}H reference images were obtained with the same setup as the 2D CSI before starting the CSI scan, so the MR images can be coregistered with 2D CSI data. The slice thickness in the T_2-weighted image was matched with the slice thickness in the 2D-CSI for coregistration.

Data Processing

Nonlocalized and 1D slice-localized Lac spectral data were processed using Bruker Xwinnmr software and lactate signals were integrated using the area under the peak. To calculate the Lac signal enhancement for the SS-SelMQC sequence, we calculated the ratio of the lactate peak area in the SS-SelMQC to the Lac peak area in the SelMQC. Although quantification of lactate can be performed by the "substitution" method (34) which was used previously (35), since these studies were done sequentially without moving the sample (phantom/tumor), there was identical coil loading and similar RF inhomogeneity and therefore these imperfections will not affect the Lac signal enhancement ratio. Signal enhancement factors are represented in terms of mean ± standard deviation. 2D ^{1}H-CSI images were reconstructed and overlaid with corresponding T_2-weighted MR image using 3DiCSI processing software (Provided by Dr. Truman Brown, Columbia University). In 2D CSI data, voxels fully filled with Lac/Lip solution (phantom) were identified and the lactate peak areas within these voxels were calculated using iterative nonlinear least-squares method using XSOS package (provided by Dr. Dikoma Shungu, Weill Medical College). The exact same voxels were analyzed from the data obtained using both sequences without considering B_1 inhomogeneity factors and coil loading factor.

RESULTS

Excitation and inversion profiles following binomial pulses were generated using an in-house computer program representing the experimental conditions. The selective excitation profile for the binomial spectral-selective pulse is shown for excitation of −2.8 ppm resonance without disturbing 0 ppm resonance (Fig. 2a) and vice versa (Fig. 2b). Similarly, the selective inversion profile of the binomial spectral-selective pulse excites the "−2.8" ppm resonance without disturbing "0" ppm resonance (Fig. 2c). In generating this figure, the Lac CH peak was referenced to "0" ppm and hence Lac CH_3 will appear at "2.8" ppm on the chemical shift. Figure 3a shows the MR image of a 5-mm thick coronal slice across the phantom showing the two compartments with Lac and Lip, respectively. Figure 3b shows the nonlocalized Lac spectra obtained using SS-SelMQC and compared with SelMQC (Fig. 3c) from the whole phantom with excellent lipid suppression. Lipid suppression was verified by choosing a slice, using SS-SelMQC and SelMQC from the lipid portion of the cylindrical phantom, and no signal was detected at the Lac/Lip frequency (data not shown as voxels spectra contain no signal). Lac signal enhancement was observed in SS-
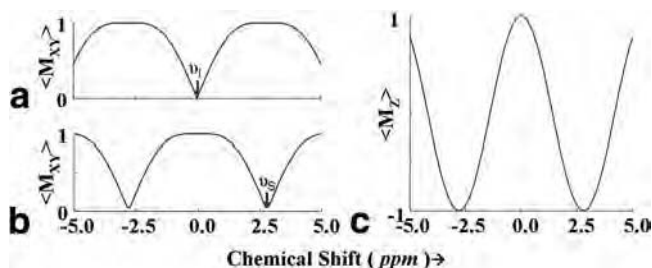
F2

F3

FIG. 2. Theoretical excitation following $\left[(\pi/4)_{\phi_1} - \Delta_1 - (\pi/4)_{\phi}2\right]$ pulse sequence for spectral selection with (ϕ_1, ϕ_2 = x, −x) **(a)** and (ϕ_1, ϕ_2 = x, x) **(b)** as a function of resonance offset. Inversion profile of for inversion of −2.8 ppm resonances shown in **(c)**. In these simulations the Lac CH peak was referenced to "0" ppm and hence Lac CH_3 will appear at "2.8" ppm on the chemical shift. RF pulse parameters and interpulse durations were chosen to match the experimental conditions given in the text.

FIG. 4. Experimental spatial-profile of lactate following the slice selective RF pulse block. TR = 3 sec, number of scans = 1, number of data points = 512, total acquisition time less than 5 min. We used 10 mM Lac/D_2O phantom for this experiment.

SelMQC over SelMQC with no significant difference in performance with respect to water and Lip suppression levels. We repeated this experiment at three different times (each timepoint corresponds to a new experiment starting with positioning, tuning, and matching) to test the consistency of signal enhancement in lactate signal from the whole Lac/Lip phantom. The integrated lactate signal area in SS-SelMQC is 2 to 3 times the lactate signal observed in SelMQC with similar suppression of lipid and water signals. Using a paired *t*-test from EXCEL software, the differences in the Lac signal were statistically significant ($P < 0.05$) between different experiments with the signal enhancement factor being 2.4 ± 0.40 in nonlocalized SS-SelMQC, compared to SelMQC. Similarly we

tested localized in vitro 1D Lac signal, which yielded similar signal enhancement factors (data not shown). Localization was achieved by applying slice-select gradient on the first spectral-selective CH_3 binomial block and its spatial profile is shown in Fig. 4.

The efficacy of this pulse sequence was also analyzed by generating lactate signals derived from localized slices. 2D chemical shift imaging data were obtained from a 10-mm sagittal slice across the phantom located at the center (covering both Lip and Lac) using both methods (data not shown). With similar water and lipid suppression, lactate signal from different voxels shows a statistically significant ($P < 0.05$) signal enhancement factor of 2.4 ± 0.29 times in SS-SelMQC, compared with the SelMQC sequence. The result is similar to the enhancement observed in the nonlocalized spectra obtained using both sequences.

The same effect was demonstrated using R3337 tumors. Figure 5a shows the stacked spectrum of lactate signal obtained from a 5-mm sagittal slice from a tumor (volume = 857 mm^3) using both sequences. From peak area integrals, the lactate signal to noise with SS-SelMQC is more than 200% that obtained with the SelMQC. We also
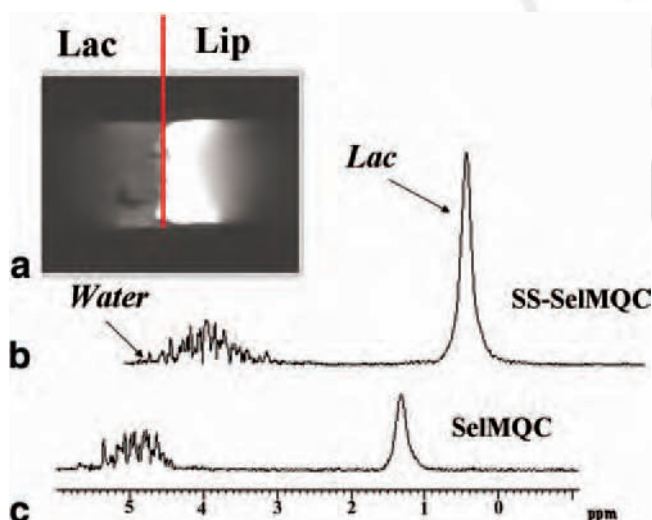
F4

F5

FIG. 3. **a:** Experimental coronal MR image obtained from lactate/lipid two-compartment phantom. Unlocalized proton spectra of lactate obtained from this phantom were compared using SS-SelMQC **(b)** and SelMQC **(c)**. Enhancement of 2.8 times was observed in SS-SelMQC compared with SelMQC. Water suppression with a new sequence is similar to that obtained with SelMQC. Data were acquired with 16 scans with TR = 2 sec. spectral width = 2500 Hz and total acquisition time was less than 2 min. Measured linewidths of Lac signal were 34 Hz, 29 Hz in **(b)** and **(c)**, respectively.

FIG. 5. **a:** Stacked plot of experimental 1D localized ^1H lactate spectrum obtained from in vivo R3327-AT tumor (volume = 857 mm^3) using SS-SelMQC and SelMQC. Experimental parameters are described in the text. **b:** 2D Lactate CSI from sagittal 5-mm thick slice using SS-SelMQC. CSI data is overlaid on T_2-contrast MR image. Chemical shift scale displayed over the tumor is between 2.5–0.5 ppm. Measured linewidths of Lac signal were 27 Hz, 25 Hz using SelMQC and SS-SelMQC sequences. Number of scans = 8, TR = 2 sec, and total acquisition time 1 hr 15 min.

obtained 16 × 16 2D-CSI lactate maps (Fig. 5b) coregistered with a T_2-weighted image corresponding to the slice shown in Fig. 5a. For comparison of both sequences, we did not move the sample between the two experiments.

DISCUSSION

Enhanced signal-to-noise ratios of metabolites are important since it will lead to decreased scan time, which is important both in clinical studies to minimize motion and patient discomfort, and in preclinical studies to minimize anesthesia, or higher spatial resolution.

Comparison of SS-SelMQC and SelMQC Pulse Sequences

Following a series of preparation RF pulses and J-evolution delays in both sequences, lipid protons in addition to lactate protons can generate MQ coherences. By applying Lac CH- and CH$_3$- frequency selective excitation pulses and CH$_3$- inversion pulse, the fraction of lipid MQ coherences that can be converted to observable magnetization was minimized. In SelMQC, frequency selective sinc pulses were applied, whereas in SS-SelMQC these pulses were replaced by binomial {1-1} pulses. We chose the ZQ→DQ pathway in both sequences resulting in observation of only 50% Lac signal. Although full Lac signal recovery is possible by adding ZQ→DQ and DQ→ZQ coherence transfer pathways using a two-step phase cycling of Lac CH pulse (28), this modification would make the method susceptible to subject motion and instrumental instabilities.

Single-slice localization in the SelMQC sequence by replacing the first frequency selective CH$_3$- excitation pulse with a broadband excitation 3-lobe sinc pulse may introduce residual MQ coherences, although it was noted by He et al. (28) that this degradation in lactate editing efficiency is not noticeable. This effect was avoided in SS-SelMQC by replacement of the slice selective RF pulse of SelMQC with a binomial pulse that removes the generation of residual lipid single quantum coherences that interferes with lactate signal and therefore reduces the lactate signal contamination. The theoretical profile for spectral selection (based on Fig. 2) has sharp transitions with ≈50 Hz range and is within the nonexcitation band. For our study, prostate tumors were implanted on the thigh region and respiration implied frequency shift is likely to be negligible. But we propose to use higher-order binomial pulses to have a broader nonexcitation region to alleviate the spectral selectivity issues due to the frequency shifts that occur due to respiration. In SS-SelMQC, by manipulating the slice gradient profile, this binomial pulse acts as a spectral-spatial pulse, although higher-order binomial pulses are desirable for improved spectral-spatial behavior.

Reasons for Signal Enhancement in SS-SelMQC

Reduced effects of J-scalar coupling evolution, molecular diffusion, as well as T_2 relaxation loss in SS-SelMQC are the likely causes of the signal enhancement observed experimentally compared to SelMQC. These effects were simulated using computer simulations of unlocalized lac-

tate signals assuming an IS spin system. Lac editing efficiency in SelMQC sequence depends on frequency selective excitation or inversion profiles, which necessitates the use of long pulses which increases the MQ evolution period and affects the lactate editing efficiency (28). In SS-SelMQC we replaced all the long frequency-selective pulses with short binomial composite RF pulses for frequency selection, which resulted in shorter MQ evolution delays. This effect increased the Lac editing efficiency by reducing J-coupling evolution as well as molecular diffusion effects as described below.

Scalar Coupling Effects

Approximately 24% of the increase in the lactate signal observed in SS-SelMQC (Fig. 6a) in comparison with SelMQC (Fig. 6b) (assuming no RF pulse imperfections) can be explained from increased scalar coupling evolution during RF pulse finite widths. We denoted RF pulse imperfection (W_1/W_1^q), where W_1 and W_1^q are actual and ideal RF field strength experienced by samples within RF coils. Hence (W_1/W_1^q) = 1 corresponds to no RF pulse imperfections and (W_1/W_1^q) = 0.9, 0.8 corresponds to the presence of 10% and 20% RF pulse imperfections, respectively. In Fig. 6a,b the X-axis is the chemical shift scale and the lactate doublet is centered on the reference chemical shift "1.32" ppm, which is the experimental frequency of CH$_3$. The peak intensity is plotted with (J ≠ 0) and without (J = 0) scalar coupling evolution considered during RF finite pulse widths in the presence of RF pulse imperfections.

FIG. 6. Computer simulated lactate spectra generated as a function of RF pulse imperfections and scalar coupling evolutions (J ≠ 0) during RF pulses using **(a)** SS-SelMQC and **(b)** SelMQC sequence. Parameters used for generating these line plots are marked on the figures. Y-axis represents percentage lactate signal normalized to 100% when there were no scalar coupling effects (J = 0) or RF imperfections. These graphs show simulated spectra of lactate CH$_3$ resonance corresponding to the 4.7T experimental conditions and assuming IS spin system for lactate (CH = I and CH$_3$ = S) with scalar coupling J_{IS} = 7 Hz.

The Y-axis denotes the Fourier transform of total transverse magnetization "M_{xy}" following the SS-SelMQC and SelMQC sequences. Lac signal intensity was normalized as 100% when there were no scalar coupling effects and RF imperfections. Introducing scalar evolution during finite pulse widths causes a decrease in Lac signal intensity to 99% in SS-SelMQC, with further reductions to 87% with 10% and 59% with 20% RF pulse imperfections. Similarly, in SelMQC, Lac signal intensity decreases to 75%, further reduces to 62% with 10% and 40% with 20% RF pulse imperfections. These simulations yielded a 24% signal gain for SS-SelMQC compared with SS-SelMQC. It should be noted that for patient studies at the clinical magnetic field strengths of 1.5T or 3.0T the signal loss due to scalar coupling effects will be more severe using SelMQC compared to SS-SelMQC. The reason for this is that frequency selective pulses used in SelMQC need to be very long, as chemical shift dispersion is very low and results in longer t_1 MQ evolution delays leading to higher signal loss. Relatively much shorter t_1 values can be maintained by binomial selective pulses in the SS-SelMQC sequence resulting in minimum scalar coupling losses increases Lac signal sensitivity. We can further minimize signal loss observed in simulations due to RF imperfections by customized RF coils generating homogeneous RF fields.

T_2 Relaxation Losses

Relatively short T_2 values of lactate have been reported in in vivo, for e.g., rat C6-glioma with 200 ms (36) and mice tumors (37) with MCa (68 ms) and Colon-38 tumors (117 ms), which would lead to lower Lac detection efficiency. Since the in vivo T_2 relaxation times are short, an optimal sequence minimizing T_2 losses is critical for accurate measurements and for absolute quantification of tissue lactate concentrations. This effect may be particularly important in studies with small tumor volumes, where lactate concentrations may be low (35), or if used for early cancer diagnosis. Since the total duration of RF pulses in the modified sequence are shorter and ≈ 45 ms less than SelMQC sequence, this enhances the lactate signal by 20% (assuming $T_2 = 200$ ms) in the SS-SelMQC method by further reducing T_2 relaxation losses.

Molecular Diffusion Effects

When two gradients are applied during the MQ evolution period to choose ZQ→DQ pathways, Lac signal attenuation occurs due to molecular diffusion of molecules during the period (28) between these gradients of duration δ ms, following the Stejskal–Tanner equation (38). We assumed phantom conditions in our calculations using the diffusion coefficient D = 1×10^{-5} cm^2 s^{-1} at room temperature. Using the equation reported earlier (28), the signal loss due to molecular diffusion is as follows:

$$S/S(0) = \exp\left[-D(p(2/\pi\gamma\delta g)\}^2\left(\Delta - \frac{1}{4}\delta\right)\right] \quad [9]$$

Where $\Delta = t_1 + \delta + de$, p is the coherence order, *de* is gradient dead time, γ is gyromagnetic ratio = 2.675e8

s^{-1}T^{-1}; for our present SelMQC parameters, the lactate signal loss will be 30% and signal loss in SS-SelMQC will be only 6%. Hence a signal gain of 24% is obtained in SS-SelMQC. The molecular diffusion losses will be severe in choosing the DQ→ZQ pathway to obtain the full signal intensity of lactate, or at low magnetic field strengths where long pulses result in higher signal loss.

Although the signal loss was calculated theoretically for individual imperfections by assuming other imperfections as zero, much higher signal loss obtained in our experiments may be due to these combined imperfection effects simultaneously in addition to magnetic field inhomogeneity effects. Signal enhancement was also confirmed from the Lac signal areas from SS-SelMQC, a single hard pulse, and SelMQC scans. We prepared 10 mM Lac/D$_2$O solution as a phantom to test the nonlocalized lactate signal obtained by one pulse (rectangular shape), SelMQC, and SS-SelMQC sequences. If we normalize lactate signal from single pulse to 100%, $\approx 50\%$ lactate signal is obtained from SS-SelMQC compared to 24% signal obtained from SelMQC using identical experimental parameters for the latter sequences (unpubl. data). The possible in vivo lactate detection limit of SS-SelMQC sequence is in the range of 2–4 mM.

CONCLUSIONS

In summary, the demonstrated ability of the SS-SelMQC sequence to measure tumor lactate in the presence of subcutaneous lipids facilitate quantitative mapping of tumor Lac distributions in in vivo tumors. With lipid and water completely suppressed in a single scan, the lactate signal can be detected by SS-SelMQC from a desired sample or slice of interest in tumor tissues that contain lipid. These results demonstrate that the SS-SelMQC sequence can detect lactate with higher sensitivity without compromising the editing efficiency of SelMQC with similar lipid and water suppression in a single scan. Lactate signal obtained from whole tumors detected by SS-SelMQC has a statistically significant ($P < 0.05$) signal enhancement of 2.4 ± 0.40 times compared to the SelMQC sequence. 1D localized and 2D CSI maps were obtained from 5-mm thick sagittal slice using SS-SelMQC and showed similar sensitivity enhancement. These preliminary studies indicate efficient selection of a slice element and clearly point out the possibilities for obtaining, via the methodology outlined here, volume selection such that the desired metabolite region of interest is excited without exciting the unwanted lipid and water resonances. We are in the process of applying higher-order binomial pulse such as {1-3-3-1} for uniform spectral-spatial behavior for slice and volume excitations. This method can be useful for carrying out studies for detecting increased glycolysis in exercised muscles and human breast cancer, as well as for lactate detection in the internal organs of transgenic animal tumor models.

REFERENCES

1. Smith IC, Princz EJ, Saunders JK. Magnetic resonance spectroscopy in cancer research. Can Assoc Radiol J 1990;41:32–38.

2. Fountas KN, Kapsalaki EZ, Gotsis SD, Kapsalakis JZ, Smisson HF 3rd, Johnston KW, Robinson JS Jr, Papadakis N. In vivo proton magnetic resonance spectroscopy of brain tumors. Stereotact Funct Neurosurg 2000;74:83–94.

3. Tosi MR, Fini G, Tinti A, Reggiani A, Tugnoli V. Molecular characterization of human healthy and neoplastic cerebral and renal tissues by in vitro ^{1}H NMR spectroscopy (Review). Int J Mol Med 2002;9:299–310.

4. Kurhanewicz J, Vigneron DB, Nelson SJ. Three-dimensional magnetic resonance spectroscopic imaging of brain and prostate cancer. Neoplasia 2000;2:166–189.

5. Zaider M, Zelefsky MJ, Lee EK, Zakian KL, Amols HI, Dyke J, Cohen G, Hu Y, Endi AK, Chui C, Koutcher JA. Treatment planning for prostate implants using magnetic-resonance spectroscopy imaging. Int J Radiat Oncol Biol Phys 2000;47:1085–1096.

6. Pirzkall A, McKnight TR, Graves EE, Carol MP, Sneed PK, Wara WW, Nelson SJ, Verhey LJ, Larson DA. MR-spectroscopy guided target delineation for high-grade gliomas. Int J Radiat Oncol Biol Phys 2001;50:915–928.

7. Zakian KL, Sircar K, Hricak H, Chen H-N, Shukla-Dave A, Eberhardt S, Muruganandham M, Ebora L, Kattan MW, Reuter VE, Scardino PT, Koutcher JA. Correlation of proton MR spectroscopic imaging with Gleason score based on step-section pathologic analysis after radical prostatectomy. Radiology 2005;234:804–814.

8. Chang J, Thakur S, Perera G, Kowalski A, Huang W, Karimi S, Hunt M, Koutcher J, Fuks Z, Amols H, Narayana A. Image-fusion of MR spectroscopic images for treatment planning of gliomas. Med Phys 2006;33:32–40.

9. Rofstad EK. Microenvironment-induced cancer metastasis. Int J Radiat Biol 2000;76:589–605.

10. Gribbestad IS, Petersen SB, Fjosne HE, Kvinnsland S, Krane J. ^{1}H NMR spectroscopic characterization of perchloric acid extracts from breast carcinomas and non-involved breast tissue. NMR Biomed 1994;7:181–194.

11. Swanson MG, Zektzer AS, Tabatabai ZL, Simko J, Jarso S, Keshari KR, Schmitt L, Carroll PR, Shinohara K, Vigneron DB, Kurhanewicz J. Quantitative analysis of prostate metabolites using ^{1}H HR-MAS spectroscopy. Magn Reson Med 2006;55:1257–1264.

12. Aboagye EO, Mori N, Bhujwalla ZM. Effect of malignant transformation on lactate levels of human mammary epithelial cells. Adv Enzyme Regul 2001;41:251–260.

13. Bhujwalla ZM, Artemov D, Ballesteros P, Cerdan S, Gillies RJ, Solaiyappan M. Combined vascular and extracellular pH imaging of solid tumors. NMR Biomed 2002;15:114–119.

14. Walenta S, Salameh A, Lyng H, Evensen JF, Mitze M, Rofstad EK, Mueller-Klieser W. Correlation of high lactate levels in head and neck tumors with incidence of metastasis. Am J Pathol 1997;150:409–415.

15. Walenta S, Wetterling M, Lehrke M, Schwickert G, Sundfor K, Rofstad EK, Mueller-Klieser W. High lactate levels predict likelihood of metastases, tumor recurrence, and restricted patient survival in human cervical cancers. Cancer Res 2000;60:916–921.

16. Gribbestad IS, Fjosne HE, Haugen OA, Nilsen G, Krane J, Petersen SB, Kvinnsland S. In vitro proton NMR spectroscopy of extracts from human breast tumours and non-involved breast tissue. Anticancer Res 1993;13:1973–1980.

17. Poptani H, Bansal N, Graham RA, Mancuso A, Nelson DS, Glickson JD. Detecting early response to cyclophosphamide treatment of RIF-1 tumors using selective multiple quantum spectroscopy (SelMQC) and dynamic contrast enhanced imaging. NMR Biomed 2003;16:102–111.

18. Quennet V, Yaromina A, Zips D, Rosner A, Walenta S, Baumann M, Mueller-Klieser W. Tumor lactate content predicts for response to fractionated irradiation of human squamous cell carcinomas in nude mice. Radiother Oncol 2006;81:130–135.

19. Aboagye EO, Bhujwalla ZM, Shungu DC, Glickson JD. Detection of tumor response to chemotherapy by 1H nuclear magnetic resonance spectroscopy: effect of 5-fluorouracil on lactate levels in radiation-induced fibrosarcoma 1 tumors. Cancer Res 1998;58:1063–1067.

20. Lee SC, Huang MQ, Nelson DS, Pickup S, Wehrli S, Adegbola O, Poptani H, Delikatny EJ, Glickson JD. In vivo MRS markers of response to CHOP chemotherapy in the WSU-DLCL2 human diffuse large B-cell lymphoma xenograft. NMR Biomed 2008;21:723–733.

21. Shkarin P, He Q. Lactate detection in human breast cancer on 2.1T MR system. In: Proc 9th Annual Meeting ISMRM, Glasgow; 2001:2327.

22. Bottomley P. Spatial localization in NMR spectroscopy in vivo. Ann N Y Acad Sci 1987;508:333–348.

23. Frahm J, Bruhn H, Gyngell ML, Merboldt KD, Hanicke W, Sauter R. Localized high-resolution proton NMR spectroscopy using stimulated echoes: initial applications to human brain in vivo. Magn Reson Med 1989;9:79–93.

24. Rothman DL, Behar KL, Hetherington HP, Shulman RG. Homonuclear 1H double-resonance difference spectroscopy of the rat brain in vivo. Proc Natl Acad Sci U S A 1984;81:6330–6334.

25. Freeman DM, Sotak CH, Muller HH, Young SW, Hurd RE. A double quantum coherence transfer proton NMR spectroscopy technique for monitoring steady-state tumor lactic acid levels in vivo. Magn Reson Med 1990;14:321–329.

26. Trimble LA, Shen JF, Wilman AH, Allen PS. Lactate editing by means of selective-pulse filtering of both zero- and double-quantum coherence signals. J Magn Reson 1990;86:191–198.

27. He Q, Bhujwalla ZM, Maxwell RJ, Griffiths JR, Glickson JD. Proton NMR observation of the antineoplastic agent Iproplatin in vivo by selective multiple quantum coherence transfer (Sel-MQC). Magn Reson Med 1995;33:414–416.

28. He Q, Shungu DC, van Zijl PC, Bhujwalla ZM, Glickson JD. Single-scan in vivo lactate editing with complete lipid and water suppression by selective multiple-quantum-coherence transfer (Sel-MQC) with application to tumors. J Magn Reson B 1995;106:203–211.

29. Hore PJ. Solvent suppression in Fourier transform nuclear magnetic resonance. J Magn Reson 1983;55:283–301.

30. Hore PJ. Nuclear magnetic resonance. Solvent suppression. Methods Enzymol 1989;176:64–77.

31. Hardy PA, Recht MP, Piraino DW. Fat suppressed MRI of articular cartilage with a spatial-spectral excitation pulse. J Magn Reson Imaging 1998;8:1279–1287.

32. Kwok WE, Totterman SM, Zhong J. 3D interleaved water and fat image acquisition with chemical-shift correction. Magn Reson Med 2000;44:322–330.

33. Peng Q, McColl RW, Wang J, Weatherall PT. Novel rapid fat suppression strategy with spectrally selective pulses. Magn Reson Med 2005;54:1569–1574.

34. Hennig J, Pfister H, Ernst T, Ott D. Direct absolute quantification of metabolites in the human brain with in vivo localized proton spectroscopy. NMR Biomed 1992;5:193–199.

35. Yaligar J, Thakur S, Lupu M, Wang Y, Matei C, Zakian K, Koutcher J. Comparative study of tumor lactate and tumor vasculature in aggressive and indolent prostate cancer animal models by 2D MR Spectroscopic Imaging and DCE-MRI. In: Proc 16th Annual Meeting ISMRM, Toronto; 2008:369.

36. Terpstra M, High WB, Luo Y, de Graaf RA, Merkle H, Garwood M. Relationships among lactate concentration, blood flow and histopathologic profiles in rat C6 glioma. NMR Biomed 1996;9:185–194.

37. Muruganandham M, Koutcher JA, Pizzorno G, He Q. In vivo tumor lactate relaxation measurements by selective multiple-quantum-coherence (Sel-MQC) transfer. Magn Reson Med 2004;52:902–906.

38. Saarinen TR, Johnson CS J. High-resolution electrophoretic NMR. J Am Chem Soc 1988;110:3332–3333.

AUTHOR QUERIES

AUTHOR PLEASE ANSWER ALL QUERIES   1

AQ1: Ref. 21 is Shkarin and He; no Pavel et al. in Refs.

AQ2: upsilon correct? Some text math did not convert; please check carefully.

1

Lactate Imaging and DCE-MRI as surrogate markers of Prostate Tumor

Aggressiveness [#]

4

5

6   J. Yaligar[1], S. B. Thakur[1,2], S. Carlin[1], H. T. Thaler[3] M. E. Lupu[1], Y. Wang[1], C. C. Matei[2], K. L.

7   Zakian[1,2], and J. A. Koutcher[1,2,4]

8

9

10   [1]Departments of Medical Physics, [2]Radiology, [3]Epidemiology and Biostatistics

11   [4]Medicine, Memorial Sloan-Kettering Cancer Center (MSKCC), New York, NY,

12   United States-10065

13

14
15
16   Running Title: *Lactate imaging and DCE-MRI in prostate tumors*

17   Key words: Lactate, R3327AT, Prostate, Tumor heterogeneity, Sel-MQC, Immunohistochemistry,

18   Dunning H

21   Corresponding Author: Jason A. Koutcher, MD, PhD
22   Dept. of Medical Physics
23   Memorial Sloan Kettering Cancer Center
24   1275 York Avenue
25   New York, New York 10065
26   212-639-8834
27   koutchej@mskcc.org
28

29 **Abstract**

30 We performed longitudinal lactate spectroscopic imaging and dynamic contrast enhanced

31 magnetic resonance imaging (DCE-MRI) studies in two prostate tumor models, the Dunning

32 R3327 AT and Dunning H, to determine the potential of lactate and DCE-MRI as markers of

33 tumor aggressiveness. Dunning R3327-AT (16 rats) and Dunning H (6 rats) were studied at five

34 different tumor volumes (groups I to V), ranging in size from 110-2453 mm^3). Lactate

35 determinations were performed with the Selective Multiple Quantum Coherence (Sel-MQC)

36 sequence. Tumor perfusion was evaluated using DCE-MRI. Lactate was not detected in small

37 (110-265 mm^3) R3327-AT tumors. Tumor lactate increased from 1.53 ± 0.54 mM (Group

38 II=478-649 mm^3) to 4.78 ± 1.66 mM (Group III; 1035-1207 mm^3), 4.64 ± 1.26 mM (Group IV;

39 1409-1708 mm^3), and decreased to 2.71 ± 0.93 mM (Group V; 1941-2453 mm^3) and was greater

40 in the core than the rim. Lactate was not detected in Dunning H tumors. Akep decreased in both

41 tumors with volume ($p<0.001$), and was greater in the rim than the core (R3327-AT ($p<0.001$);

42 Dunning H ($p<0.023$)). Dunning H tumors had higher Akep values than R3327-AT tumors

43 ($p<0.001$) demonstrating better perfusion. Lactate is not detected in small Dunning R3327 AT

44 tumors but increases with growth and subsequently decreases. This increase in lactate in the

45 Dunning R3327-AT occurs with concomitant decreases in Akep and evolving differences in

46 perfusion between the rim and core, indicating poorer perfusion. Lactate is not detected in slow

47 growing Dunning H tumors suggesting it as a potential biomarker for aggressive tumors.

48

49 **Abbreviations:** 2D-CSI, 2 dimensional-chemical shift imaging; DCE-MRI, dynamic contrast-

50 enhanced magnetic resonance imaging; HIF, hypoxia inducible factor; MRSI, magnetic

51 resonance spectroscopic imaging; Sel-MQC, selective multiple quantum coherence.

52   **Introduction**

53   Patients with the identical pathological cancer diagnosis often have different clinical courses.

54   This unexplained heterogeneity is particularly true of prostate cancer, a disease which is usually

55   indolent, yet sometimes follows an aggressive course. Discriminating between patients with

56   aggressive vs. indolent prostate cancer is a major clinical problem and often leads to patients

57   being overtreated [1-2]. Nomograms are useful to predict outcomes and for selecting patients for

58   watchful waiting [3-4] but are imperfect, and newer biomarkers with higher predictive value are

59   necessary to add to, and improve upon clinical parameters (PSA, Gleason grade, stage etc).

60

61   In addition to tumor heterogeneity between patients, within a specific tumor there are metabolic,

62   physiologic and genetic differences between cells, which can cause treatment failure and

63   metastases. Clonal evolution and changes in the tumor microenvironment during tumor growth

64   can lead to the development and selection of cells with more malignant phenotypes [5-6].

65   Changes in tumor physiology can induce hypoxia which can cause preferential selection of cells

66   with p53 mutations and greater metastatic potential [7-8], tumor progression [9], and resistance

67   to anti-neoplastic treatments [10-11]. Detecting local areas of resistance to treatment with new

68   more accurate biomarkers would allow targeting of these areas with local therapies or higher

69   radiation doses [12], to eradicate resistant cells. Lactate has been recognized in cervical cancer

70   and head and neck tumors as a marker of a higher risk of metastases and poor prognosis [13-14].

71

72   Changes in lactate have also been suggested to be an early marker of response [15], [16].

73   Tumors evolve with growth and therefore a non-invasive biomarker might be important for

74   repetitive non-invasive assays of the tumor. With the widespread use of MRI and emerging use

75 of MRSI in prostate cancer staging [17-18], a modification to existing pulse sequences could

76 readily non-invasively detect lactate.

77 The Dunning R3327-AT tumor is an aggressive, highly anaplastic prostate cancer with a

78 doubling time of 3.3 days which was derived from a Dunning R3327-H tumor, a well-

79 differentiated, hormone responsive tumor with a doubling time of 12-20 days. The well-

80 differentiated, slower growing Dunning H has higher oxygen levels [19] compared to anaplastic

81 R3327 AT tumors, longer radiation induced growth delays [20], and lower pimonidazole binding

82 (5%) compared to R3327-AT tumor (18%; $p<0.05\%$) [21]. Therapeutic and histological

83 characteristics of these tumors are similar to human prostate adenocarcinomas [20].

84
85 Imaging lactate *in vivo* by magnetic resonance is feasible but challenging since the methyl

86 resonance of lactate is co-resonant with the methyl resonance of lipids. The scalar (J) coupling

87 between the doublet at 1.3 ppm arising from the methyl (CH_3) protons and the quartet at 4.1 ppm

88 arising from the methine proton (CH) is used to selectively detect the lactate signal [22-24]. The

89 selective multiple-quantum coherence transfer (Sel-MQC) [25] sequence with phase encoding

90 was used to generate lactate maps.

91

92 The aim of this study was to compare the concentration of lactate in aggressive and indolent

93 prostate tumor model to determine its potential as a marker of tumor aggressiveness.

94 Specifically, the goals were to (a) quantitatively compare the whole tumor lactate concentration

95 in Dunning R3327-AT and Dunning H prostate tumor models to determine the potential of

96 lactate as a marker of tumor aggressiveness, (b) evaluate spatial heterogeneity of lactate and c)

97 evaluate tumor perfusion and permeability in both tumor models using dynamic contrast

98 enhanced MRI (DCE-MRI).

99 **Experimental Methods**

100 *Animal model and cell culture*

101 Animal studies were conducted in compliance with protocols approved by the Institutional

102 Animal Care and Use Committee (IACUC) of Memorial Sloan-Kettering Cancer Center

103 (MSKCC). Dunning R3327-AT cells were seeded in 75 cm^2 flask and grown in 20 ml

104 Dulbecco's Modified Essential Medium (DMEM) containing 4.5 g/L of Glucose and L-

105 glutamine without sodium pyruvate and supplemented with FCS (10%), Penicillin and

106 Streptomycin (1 %) were added under sterile conditions at 37 ^{0}C in a 95 % humidified air and 5

107 % carbon dioxide atmosphere. Trypsin (0.05%) with 0.53 mM EDTA, HBSS without calcium

108 and magnesium salts was used to separate the cells. Copenhagen rats (Charles River

109 Laboratories) were implanted with $5x10^6$ cells subcutaneously in the thigh region. Dunning H

110 tumor was generously provided by Drs. Susan Dalrymple and John Isaacs from Johns Hopkins

111 School of Medicine and tumors were grown by implanting 2 mm sections of tissue

112 subcutaneously in the thigh of Fischer-Copenhagen rats (Harlan Sprague Dawley).

113

114 Tumor-bearing rats were studied longitudinally and the data grouped based on measurements

115 performed at similar tumor volumes. For the Dunning R3327-AT tumor, the groups were 110-

116 265 mm^3 (I), 478-649 mm^3 (II), 1035-1207 mm^3 (III), 1409-1708 mm^3 (IV) and 1941-2453 mm^3

117 (V). For the Dunning H models, the studies were similarly grouped as 227-259 mm^3 (I), 430-546

118 mm^3 (II), 1000-1236 mm^3 (III), 1382-1715 mm^3 (IV) and 1886-2255 mm^3 (V). Tumor volume

119 (V) was calculated as V= $(\pi/6)*$ x $*$ y $*$ z; where x, y and z are the length, breadth and vertical

120 depth of the tumor, correcting for the skin thickness of 1.3 mm [20]

121

122 ***MR Experiments***

123 Tumor bearing rats were anesthetized with Isoflurane (1.0 - 2.5 %) combined with air during

124 catheterization and MR experiments. A tail vein catheter (24G X ¾" (Terumo Medical

125 Corporation, Elkton, M.D) was inserted prior to placing the rat in the magnet. MR experiments

126 were performed on a Bruker 4.7 T, 40 cm bore animal scanner. A home-made 2 turn solenoid (25

127 mm diameter) was used as transmitter/receiver for all studies. Three perpendicular scout images

128 were obtained (Field of view (FOV)=15 cm, slice thickness 5 mm, repeat interval (TR) = 100

129 ms, echo time (TE) = 5 ms) for positioning of the animal to ensure that the tumor was in the

130 center of the magnet. Using the tri-pilot scans as a spatial reference, a spin-spin (T2) weighted

131 MR image (sagittal orientation) of 5 mm slice thickness was collected using the Multi Slice

132 Multi Echo (MSME) sequence (TR-3734 ms, TE- 30ms, a 512 X 128 matrix size, 1 slice and 2

133 excitations).

134

135 Lactate detection was performed using the Selective Multiple Quantum Coherence (Sel-MQC)

136 editing sequence [25], using frequency selective 15 ms single-lobe Sinc pulses. The zero

137 quantum (ZQ)→double quantum (DQ) coherence transfer pathway was selected using a phase

138 cycling gradient scheme with g1:g2:g3 = 0:-1:2 where g1, g2, and g3 are the relative gradient

139 strengths with respective durations $\delta_1 = \delta_2 = 2$ ms, $\delta_3 = 4$ ms, and an amplitude of 24 G/cm. Five

140 hundred twelve data points were collected with 8 averages, TR=2s, and spectral width of

141 2500Hz. Localization was achieved using a 16×16 phase encoding matrix, and a FOV=40 mm

142 (2.5x2.5 mm in plane resolution). The voxel volume was 31.2 mm^3 and total 2D-CSI (two

143 dimensional chemical shift image) acquisition time was 75 minutes. Two dimensional CSI maps

144 of lactate were obtained from a 5 mm slice in the tumor which was coregistered with the 5 mm

145   thick T2-weighted image. For quantitation using the substitution method [26], a 9.12 cm^3

146   cylindrical reference phantom containing 30 mM lactate and 25uM Gd-DTPA was scanned with

147   identical parameters.

148

149   Upon completion of the MRSI lactate study, DCE-MRI imaging was done. A pre-contrast proton

150   density sagittal MR image (3 slices, slice gap=0.20 mm) was obtained by using a Gradient Echo

151   Fast Imaging (GEFE) sequence with TR/TE=500ms/3ms, 30° flip angle, 2 mm slice thickness,

152   4cm FOV, 128 X 128 matrix size, and 2 excitations. Subsequently the dynamic spin lattice (T1)

153   weighted MR images were obtained using the same sequence/parameters as in the pre-contrast

154   proton density images except that the TR was reduced to 50ms, 12 sec temporal resolution, 96

155   time points, and 30° flip angle. Gd-DTPA (0.2 mM/kg; Magnevist, Berlex Laboratories) was

156   injected intravenously after the first 10 images of the dynamic sequence were acquired and these

157   images were used to measure the pre-contrast signal intensity under saturation conditions.

158
159
160
161   ***MR Data Processing***

162   DCE-MRI data were analyzed using the two compartment model of Hoffman et al [27] to

163   evaluate the rate constant k_{ep} (rate constant for Gd moving from the interstitial space to plasma) ,

164   Ak_{ep} (A - Amplitude in the model) on a voxel-by-voxel basis using in house IDL programs. In

165   each tumor, the analysis was performed on data from 3 slices, each 2mm thick.

166

167   The MRSI data underwent a two dimensional spatial Fourier transform and the spectral grid was

168   superimposed on the corresponding T2-weighted image using the 3DiCSI software package

169   (courtesy of Truman Brown, Ph.D., Columbia University). The voxels within the tumor were

Lactate imaging and DCE-MRI in prostate tumors

170   identified and the free induction decay (FID) from each tumor voxel was extracted. The FID was

171   used as input to the JMRUI (Java Magnetic Resonance User Interface) software package [28]

172   and the lactate resonance was fit in the time domain using AMARES (Advanced Method for

173   Accurate, Robust and Efficient Spectral fitting). The 2D-CSI data set from the reference

174   phantom used for lactate quantitation (see below) was processed similarly. For quantitation,

175   each tumor voxel was referenced to a phantom voxel at the exact same location. The tumor voxel

176   lactate peak area, the reference voxel lactate peak area, the appropriate T1 saturation factors and

177   the comparative coil loading parameters for tumor and phantom studies were used to quantify the

178   tumor voxel lactate according to the following equation:

179

$$\text{Unknown concentration} = \frac{\text{Integration area of unknown X Concentration of reference standard X } (V_{ref}/V_{test})}{\text{Integration area of reference standard X } 1\text{-}e^{(-TR/T1)}}$$

180

181   where (V_{ref}/V_{test}) is ratio of the voltage difference of reference sample to test sample and

182   T1 is the spin-lattice relaxation of lactate. Lactate in the doped phantom was fully relaxed. In-

183   vivo T1 measurements of lactate were done by introducing a nonselective 180˚ sinc pulse to the

184   Sel-MQC sequence [29] with inversion recovery delays from 10 ms to 6 sec. The T1 value for

185   the R3327-AT tumor (volume=1533 mm^3) was 1.26 ± 0.15 sec

186

187   To evaluate the lactate distribution in the tumor core and rim, we analyzed lactate in both the rim

188   (single layer of outside voxels that are completely in the tumor) and the core (all other voxels

189   inside the tumor) separately. Those voxels were also used to define rim and core for the DCE-

190   MRI studies, despite the difference in voxel sizes between the two techniques.

191

192

Lactate imaging and DCE-MRI in prostate tumors

193 **MR Data Statistics**

194 We obtained scans for each rat at two to five time points. Lactate level and Akep were

195 determined for each voxel from each MRSI image. Lactate was recorded as a numerical value,

196 or as zero if the peak was not detected. Since there were a large number of voxels where lactate

197 was not detected, especially in small tumors, either treating them all as zero or excluding them

198 from computations would introduce bias. Therefore, we assumed that the log-lactate levels were

199 normally distributed, and that any voxel without detectable lactate was considered to be <

200 1.2mM, which was the smallest non-zero value observed in the entire experiment. Lactate and

201 Akep data were analyzed using the generalized linear model.

202

203 Measurements were obtained for varying numbers of voxels within each tumor scan, and voxels

204 were classified as located in the core (C) or rim (R) of the tumor. The statistical model assumed

205 that 1) the expected value of lactate followed a quadratic function of tumor volume, 2) there was

206 random variation among rats in a) the tumor volume at which lactate reached a peak and b) the

207 magnitude of the peak, 3) there was a proportional difference between typical values for core

208 voxels vs. rim voxels, and 4) the variation in measurements within a region of interest followed a

209 censored log-normal distribution. We applied a non-linear mixed effects statistical model using

210 Proc NLMixed (SAS version 9). Two rats with no detectable lactate in any scan yielded no

211 useful information and were excluded from the analysis. Analysis of Akep values was more

212 straightforward because there were very few zero values. Analysis of covariance was used after

213 applying a square root normalizing transformation.

214

215

216

217 **HISTOLOGY**

218 *Immunohistochemical staining*

219 Four rats with Dunning R-3327-AT tumors were sacrificed following serial MR examinations for

220 measurements of tumor necrosis and hypoxia. Since initially all the MR experiments were

221 performed serially resulting in only large tumors being available for analysis, an additional 4 rats

222 were studied by MR, each at a single time point and sacrificed, to obtain an estimate of necrosis

223 and lactate at small and medium tumor volumes. Six additional rats were sacrificed at various

224 tumor volumes without undergoing MR studies specifically to provide estimates of the variation

225 of tumor necrosis with volume

226

227 After the final MRSI experiments, tumors studied by histology and immunohistochemistry were

228 excised, snap-frozen in isopentane/dry ice, embedded in cutting medium (OCT 4583, Sakura

229 Finetek) and 8 μm-thick contiguous frozen sections from multiple locations within the tumor

230 obtained using a cryostat microtome (Microm International GmbH). Sections were fixed in 4%

231 paraformaldehyde solution for 10 minutes at room temperature then blocked in Superblock-PBS

232 (Pierce, USA) for 1 hour, followed by either immunofluorescence staining for pimonidazole

233 distribution, or haematoxylin/eosin for determination of tumor necrosis. To determine the

234 relationship between viable tissue volume and lactate, the necrotic tumor fraction was excluded

235 for these calculations by estimating the percent necrotic area on 5 histological sections taken

236 from separate regions of each tumor. Pimonidazole staining was carried out as described

237 previously [30] . As a control for non-specific antibody binding, some sections were stained with

238 non-specific mouse IgG conjugated to FITC.

239

240   Images of pimonidazole stained tumor sections were acquired at high magnification (x100) using

241   an Olympus BX40 fluorescence microscope (Olympus America Inc., Melville, NY) equipped

242   with a motorized stage (Prior Scientific Instruments Ltd., Cambridge, UK) and an appropriate

243   filter. The individually captured image frames were rendered into a montage of the entire tumor

244   section using ImagePro software (Media Cybernetics Inc, Bethesda, MD).

245

246   ***Histological Data Analysis***

247   For determination of tumor necrotic fraction, images of whole tumor sections stained with

248   haematoxylin/eosin were examined using Photoshop 7.0 software. Fractional areas of necrosis

249   were determined subjectively for each section by two investigators, and results were pooled.

250   Sections from at least 3 different locations within a single tumor were used to determine the

251   mean tumor necrotic fraction.

252

253   For determination of mean pimonidazole binding fraction, immunofluorescence images of anti-

254   pimonidazole images were converted to binary form using a threshold determined from the

255   staining intensity observed in tumor sections stained with the control antibody. This threshold

256   remained constant for all tumors analyzed. The percentage of tumor area with staining intensity

257   greater than the threshold value was then determined using Photoshop 7.0 software. Sections

258   from at least 3 different locations within a single tumor were used to determine the mean tumor

259   pimonidazole-positive fraction.

260
261
262
263
264
265

266 **Experimental Results**

267 *In-vivo lactate measurement*

268 The anaplastic, faster-growing R3327-AT cell line had an in vivo tumor doubling time (TDT) of

269 3.3 ± 0.17 days. The well-differentiated, slower growing Dunning H had a doubling time of 22.8

270 ± 1.95 days (Figure 1) (p<0.001), compatible with previous studies [20].

271

272 Figure 2A shows a series of T2 weighted MR images of 5mm thickness co-registered with 2D-

273 CSI lactate spectra obtained on the Dunning R3327 AT tumor. Lactate peaks in the tumor region

274 are highlighted. Lactate was not detected in R3327-AT tumors studied in the volume range 110-

275 265 mm^3 (group I; data not shown). As tumor volumes increased to the range of 478-649 mm^3

276 (group II), the average voxel lactate concentration detected was 1.54 ± 0.54 mM (Fig 3A). In

277 group III (tumor volume 1035-1207 mm^3), the lactate concentration increased to 4.79 ± 1.67

278 mM. In Groups IV (1409-1708 mm^3) and V (1941-2453 mm^3), lactate was 4.64 ± 1.26 mM and

279 2.71 ± 0.93 mM respectively (Fig 3A, Table 1). The variation of average lactate concentration

280 with growth is shown graphically in Figure 3A and demonstrates the initial increase and

281 subsequent decrease in lactate noted with tumor growth. Results of the non-linear mixed effects

282 analysis showed very significant curvature in the relationship between lactate and tumor volume

283 (p=0.008) namely, an initial increase followed by a decrease after reaching a peak that varied

284 among rats at volumes of 1048 +/- 467 (SD) mm^3. There was a significant quadratic or peak

285 effect in the relationship between lactate per voxel and tumor volume (p<0.001) in the R3327-

286 AT tumor with significant variation among rats in the volume at which the maximum expected

287 value of (log) lactate occurred.

288

289   When the lactate concentration in the outer voxels of the tumor ("rim") was compared to all the

290   other voxels ("core") (Fig. 3B), lactate was significantly higher in the core compared to the rim,

291   independent of tumor volume (p<0.001). The lactate concentration vs tumor volume curve for

292   the core, rim and whole tumor increases to a maximum followed by a decrease after reaching a

293   peak or plateau in groups III and IV. This was characterized by a quadratic term in the statistical

294   model, with a coefficent that was significantly less than zero, reflecting a downturn in lactate

295   concentration with volume after a peak. Inclusion of an additional parameter in the statistical

296   model indicated weak evidence (p=0.09) that on average, the lactate maximum concentration

297   occurred at larger tumor volumes for the core voxels compared to the rim.

298

299   A representative set of 2DCSI spectra of Dunning H prostate model at different volumes is

300   represented in Figure 2B (groups I to V). Lactate was not detected in any tumor, regardless of the

301   volume.

302
303
304
305   ***DCE-MRI analysis***
306
307   Dunning R3327-AT

308   The average Akep for group I tumors was 1.59 ± 0.53 /min. With an increase in tumor size (478

309   - 649 mm^3), Akep decreased to 0.65 ± 0.12. With further increases in tumor size, the Akep value

310   for group III and IV tumors were 0.55 ± 0.11 and 0.36 ± 0.04 respectively. The largest tumors

311   (group V) had a value of Akep of 0.34 ± 0.05 (Fig. 4A; Table 2A).

312

313   We analyzed whether the rim and core Akep measurements differed. The same criterion for

314   classifying the rim and core voxel was adopted as was used in the lactate analysis (Fig. 4B). The

Lactate imaging and DCE-MRI in prostate tumors

315   average tumor rim and core Akep value of the lowest tumor volume cohort were 1.61 ± 0.52

316   /min vs. and 0.15 ± 0.14 /min respectively, but only one of the 4 animals had a tumor large

317   enough to delineate core voxels so the biological significance of this difference is unclear.   With

318   the increase in tumor volume to 478-649 mm^3, the tumor rim and core Akep values were 0.71 ±

319   0.12 /min vs. 0.27 ± 0.07 /min.   As expected, there are a greater number of voxels in the rim

320   than in the core. At higher tumor volumes (1035-1207 mm^3 and 1409-1708 mm^3), the rim and

321   core Akep values decreased to 0.63 ± 0.12 /min vs 0.36 ± 0.12 /min and 0.50 ± 0.07 /min vs 0.15

322   ± 0.03 /min respectively. At the largest tumor volumes the rim and core Akep values were 0.47 ±

323   .07/min and 0.14 ± 0.02/min respectively.   The rim Akep values were significantly higher than

324   core values for the Dunning R3327-AT tumors (p<0.001)

325

326   ***DH tumors***

327   Slow growing Group I Dunning H tumor had an average Akep value of 1.23 ± 0.12/min (Fig.

328   5A, Table 2B). This decreased to 1.06 ± 0.23/min, 0.84 ± 0.21/min and 0.86 ± 0.08/min in

329   groups II, III and IV tumors respectively. With continued tumor growth, the whole tumor Akep

330   values decreased (Group V = 0.46 ± 0.04/min). We subsequently subdivided the analysis to

331   study the rim and core as we had done previously for the Dunning R3327-AT tumor except in

332   the Group I tumors wherein there were no core voxels because of the small tumor size. The rim

333   and core Ak$_{ep}$ values both decreased with growth (p<0.001).

334

335   The Dunning H exhibited heterogenous perfusion as manifested by significant differences in

336   Akep value between the rim and core (p<0.023). The Dunning H tumors had significantly higher

337   Akep values than the R3327-AT tumors, as measured in the whole tumor (p<0.001), the core

338   (p<0.001) and the rim (p<0.001). Akep declined progressively over the range of tumor sizes in

339   the Dunning H tumors (p<0.001), particularly at the largest tumor volumes. After applying an

340   appropriate normalizing transformation to Akep (e.g., cube root), the rate of decrease was linear.

341   This decrease was also noted if the data were analyzed separately for the rim and core (p<0.001).

342

343   ***Histology and Immunohistochemistry Correlation***

344   The Dunning R3327-AT tumors have necrosis present even at small tumor volumes (Fig. 6a, b,

345   Fig. 7A). In contrast, the Dunning H tumors had no observable necrosis even at volumes

346   approaching 2300 mm^3, (Figure 6c). In the R33327-AT tumor, we found that with increasing

347   tumor volume, the necrotic fraction increased significantly ($R^2 = 0.808$; p <0.001) (Fig, 7A). A

348   linear correlation between the concentration of lactate measured and the <u>viable</u> tumor volume

349   was noted indicating that the concentration of lactate increases with tumor growth corrected for

350   viability ($R^2 = 0.764$; p=0.005). (Figure 7B)

351

352   Tumor sections sequential to those used for histological staining were assessed for the

353   distribution of the hypoxia tracer pimonidazole by immunofluorescence staining (Fig. 6(d), (e),

354   (f)). We observed that the fractional pimonidazole-positive tumor area increased with tumor

355   volume ($R^2 = 0.720$, p = 0.007). Comparison of pimonidazole-positive tumor fraction to lactate

356   values also showed a statistically significant positive correlation ($R^2 = 0.602$, p = 0.023; Fig.

357   7C).

358   **Discussion**

359   *Tumor lactate kinetics in R3327 AT model*

360   Tumors have increased lactate levels, due to increased production and/or decreased clearance. Based on

361   this study of two prostate tumor models with different growth rates, necrosis, and radiation

362   sensitivity [20], we hypothesize that lactate is a potential marker of prostate tumor

363   aggressiveness. Lactate concentrations have been shown to have prognostic value [13], [14] [31]

364   [32] in other tumors, and have correlated with a high probability of metastasis and decreased

365   patient survival.

366

367   In this study, lactate was not detected in the Dunning R3327-AT at small tumor volumes (110 –

368   265 mm^3). At the lowest tumor volumes, the tumor appears to be effectively and uniformly well

369   perfused, based on the measurements of both lactate and Akep, suggesting adequate oxygen and

370   nutrient delivery to meet the metabolic requirements of the tumor.   As the R3327-AT tumor

371   volume increased, lactate was detected and was associated with a concomitant decrease in Akep

372   and metabolic and perfusion heterogeneity, suggesting that the tumor has evolved into a more

373   metabolically deprived state associated with poorer perfusion. The perfusion and metabolic

374   deficits become more pronounced as tumor growth continues and is compatible with induction of

375   hypoxia (Fig. 6e) and the tumor being forced to undergo increasing anaerobic glycolysis with

376   increased lactate production.

377

378   In contrast, in the Dunning H lactate is not detected and there is a significant drop in Akep

379   primarily at the highest tumor volume range. The Akep values were approximately constant

380   between 1000 and 1700 mm^3. These relatively constant values of Akep in this volume range are

Lactate imaging and DCE-MRI in prostate tumors

381 noted both in the rim and the core of the tumor (Fig. 5, Table 2B).   These data explain the lack

382 of necrosis, hypoxia and lactate in this model. We hypothesize that the relative absence of lactate

383 in the Dunning H is due to the better perfusion, minimizing hypoxia, anaerobic glycolysis, and

384 necrosis.   The absence of lactate at very large tumor volumes wherein perfusion has decreased

385 (although the decrease in Akep is not as large as in the Dunning R3327-AT) may be due to the

386 slower growth rate of the Dunning H which would place a lower demand on energy requirements

387 and therefore lower glucose requirements. A major cause of the differences in the tumor models

388 may be ascribed to differences in perfusion as measured by Ak_{ep} which is significantly higher in

389 the Dunning H than in the R3327-AT.

390

391 Lactate was detected prior to the presence of significant histologic necrosis (Fig. 7A) in the

392 R3327-AT tumor indicating that the lactate is not solely due to the presence of necrotic tissue.

393 Figures 3A and 7A demonstrate that lactate decreases at larger tumor volumes where necrosis

394 becomes more significant, indicating that lactate is produced in viable tissue. In addition, there

395 is a linear increase in lactate as viable tumor volume increases, further indicating that lactate

396 occurs independently of necrosis.

397

398 Previous in vitro studies have indicated that lactate is elevated in prostate cancer [33], [34] [35].

399 Using hyperpolarized 13C spectroscopic imaging, Chen et al [36] studied the transgenic

400 adenocarcinoma of mouse prostate (TRAMP) and found that after infusion of 13C labeled

401 pyruvate, lactate could be detected in both primary and metastatic prostate tumors. Albers et al

402 [37] correlated lactate levels with a histologic index developed by the authors and suggested that

403 lactate levels increased as the tumor grade increased, as measured by their histologic index.

404

405   Numerous recent studies have shown that tumor hypoxia and altered metabolism are

406   interconnected. Hypoxia is known to enhance glycolytic activity, and likely works via the HIF1-

407   α pathway. HIF1- α is increased under hypoxic conditions and increases the expression of

408   numerous genes related to glucose metabolism including glucose transporters [38], glycolytic

409   enzymes [39] and also suppresses the activity of the citric acid cycle. Recent studies have

410   demonstrated that HIF1- α causes overexpression of pyruvate dehydrogenase kinase-1 (PDK-1)

411   [40-41] which lowers pyruvate dehydrogenase (PDH) activity. Loss of PDH activity suppresses

412   conversion of pyruvate to acetate thereby diminishing citric acid cycle activity, oxidative

413   phosphorylation, oxygen consumption and formation of reactive oxygen species (ROS). In vivo

414   lactate measurements, could be used to monitor the activity of targeted drugs aimed at inhibiting

415   various metabolic pathways, and used to determine an appropriate dose and validating it in

416   patients by monitoring lactate and changes in its concentration.

417

418   In addition to verifying that a drug is active at the target site, the in vivo measurement of lactate

419   in prostate cancer could yield both a prognostic marker as has been shown previously [37] and

420   would potentially be useful for "dose painting" by detecting areas of potential hypoxia and/or

421   radiation resistance [42-43]. One of the major advantages to obtaining localized lactate data

422   instead of measurements from the whole tumor is the ability to delineate the heterogenous state

423   of the tumor as shown in this study and potentially applying it for local therapies.

424

425   Prostate cancer is a very important tumor to study because of its high incidence associated with a

426   high survival rate, and often indolent course. Studies have demonstrated that many patients with

Lactate imaging and DCE-MRI in prostate tumors

427   prostate cancer do not need treatment since it does not alter the outcome of the disease [44].

428   There are currently no reliable methods of selecting these low risk patients and this is an area of

429   intense ongoing research [45]. The current study suggests that measurements of lactate in

430   prostate tumors might be an additional appropriate biomarker for investigations and inclusion

431   with other clinical parameters into nomograms. Since proton MRSI data of the prostate is often

432   obtained in the course of staging workup after diagnosis, these data are readily translated to the

433   clinic. Lactate editing methodologies do not require contrast agents or isotopic injection and are

434   likely to be sensitive enough to detect lactate in patients [46-48]. The use of 13C hyperpolarized

435   MRSI [37] would significantly enhance the technique, if it receives clinical approval.

436

437   Estimation of tumor hypoxic percentage (using pimonidazole immunofluorescence staining)

438   showed a positive correlation with increasing lactate in R3327-AT tumors (Fig. 7C)). In keeping

439   with previous studies [21], we were unable to detect either significant pimonidazole uptake or

440   lactate in any of the Dunning-H tumors examined**.** Taken together, these observations are

441   supportive of the hypothesis that hypoxic tumor tissue is a significant source of tumor lactate

442   production. However, as the pimonidazole-positive tumor area also increases with tumor volume

443   in the R3327-AT, it is also possible that increasing tumor volume with inadequate angiogenesis

444   is a contributing cause to lactate production.

445

446

447

448

449

450 **Conclusion**

451   Lactate is not present in the slowly growing Dunning H but is detected in a heterogenous pattern

452   in the fast growing R3327-AT tumor, suggesting that in vivo lactate measurements could be a

453   marker of aggressive tumors. Based on the tumor heterogeneity in lactate concentration, we

454   hypothesize that localized areas of aggressive, hypoxic tumors could be potentially delineated for

455   localized therapy. The core of the tumor is prone to accumulate more lactate than the rim of the

456   tumor, probably since the core of the tumor would be expected to have a less adequate oxygen

457   and blood supply. This observation is supported by the DCE-MRI study where the tumor core is

458   significantly less well perfused than its rim in the R3327-AT tumor.

459

460

465

466

467

468   **Figure Captions**

469   Figure 1. Tumor volume (mean ± SEM) measurements of Dunning R3327 AT (A) and Dunning

470   H (B) tumors. Note different time scales

471

472   Figure 2A. 2DCSI lactate spectra of R3327 AT prostate tumor model as a function of tumor

473   volume, I:613 mm^3, II:1054 mm^3, III:1455 mm^3 and IV: 2207 mm^3. T2 weighted saggital MR

474   tumor image is co-registered with 2DCSI lactate spectra. The peak intensity of the lactate

475   resonance is heterogenous, even within a specific tumor.

476

477   Figure 2B. 2DCSI lactate spectra of Dunning H prostate tumor model as a function of tumor

478   volume, A: 246 mm^3 B:512 mm^3, C:1075 mm^3, D:1382 mm^3 and E: 2255 mm^3. T2 weighted

479   saggital MR tumor image is co-registered with 2DCSI lactate spectra. Note the absence of

480   lactate in any of the voxels

481

482   Figure 3A. Measurement of average lactate in R3327 AT tumor model as a function of tumor

483   volume. Tumors in the volume range of 110- 265 mm^3 did not show lactate

484

485   Figure 3B. Evaluation of tumor core/rim lactate of R3327 AT tumor model as function of tumor

486   model (solid filled bar plots= core lactate; empty bar plots= rim lactate). Lactate initially

487   increases, shows a plateau, and then decreases in the whole tumor, rim, and core

488

489   Figure 4A. Whole tumor average Akep (/min) of Dunning R3327 AT tumor model as a function

490   of tumor volume. Akep decreases with tumor volume

491   Figure 4B. Evaluation of tumor core/rim Akep (/min) of Dunning R3327 AT tumor model at

492   different tumor volumes.

493

494   Figure 5A. Whole tumor average Akep (/min) of Dunning H tumor as a function of tumor

495   volume.

496

497   Figure 5B. Evaluation of tumor core/rim Akep (/min) of Dunning H tumor model over the

498   volume range studied.

499

500   Figure 6. H & E staining of (a) Dunning R3327 AT (118 mm^3), (b) Dunning R 3327-AT (2207

501   mm^3) and (c) Dunning H (1949 mm^3). Corresponding slides showing pimonidazole staining are

502   displayed in (d), (e) and (f).

503

504   Figure 7A. A graph of percentage of necrosis as a function of tumor volume demonstrates a

505   significant linear correlation between these two parameters.

506

507   Figure 7B. A graph of the variation of tumor lactate vs. viable tumor volume demonstrating a

508   significant linear correlation. Lactate is noted to increase with tumor growth, when corrected by

509   eliminating the necrotic tissue

510

511   Figure 7C. Graph of pimonidazole positive fraction as a function of measured lactate showing a

512   linear correlation between pimonidazole and lactate concentration. The data suggest that lactate

513   is a potential surrogate for measuring tumor hypoxia in this model.

514 Table 1 Average lactate concentration and numbers of CSI voxels in the Dunning R-3327-AT
515 tumor
516

Tumor Group	Tumor volume (mm^3)	Whole tumor		Core		Rim	
		Lactate (mM/L)	Avg # voxels	Lactate (mM/L)	Avg # voxels	Lactate (mM/L)	Avg # voxels
I	110-265	0	7	0	1	0	6
II	478-649	1.54	13	1.79	3	1.46	10
III	1035-1207	4.79	17	6.95	6	3.68	11
IV	1409-1708	4.64	20	7.34	8	3.02	12
V	1941-2453	2.71	24	4.78	10	1.40	14

517
518

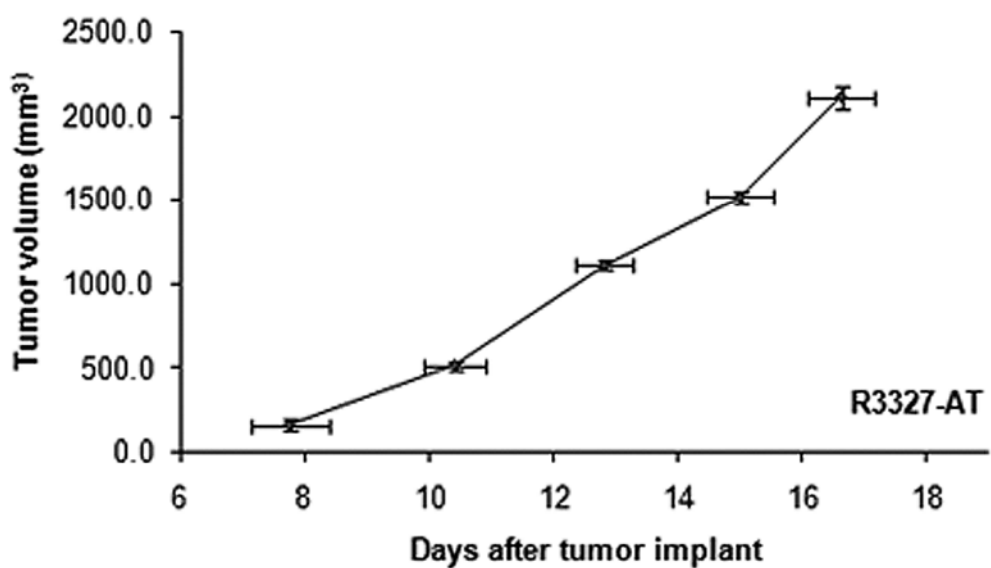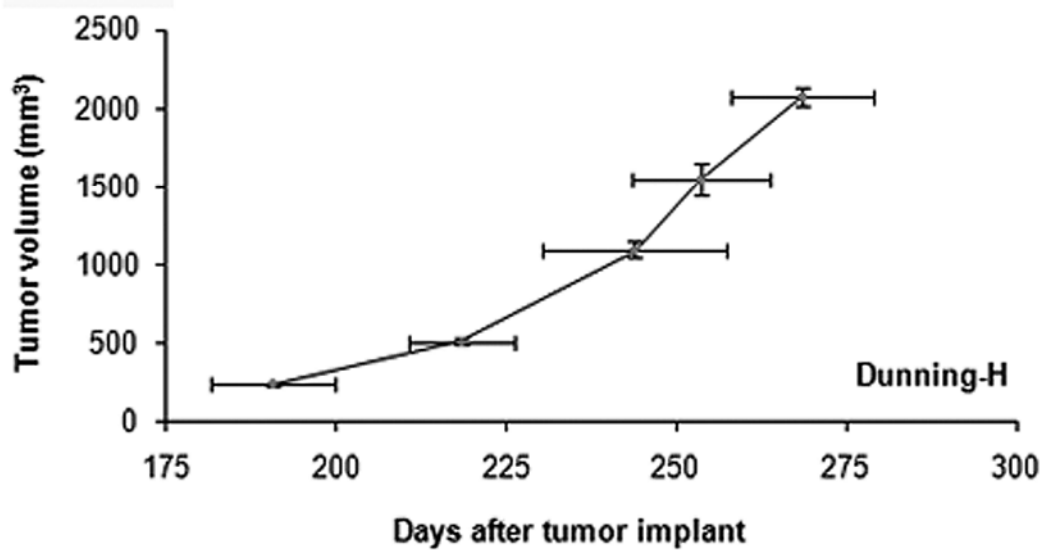*Lactate imaging and DCE-MRI in prostate tumors*

519   Table 2A Average Akep values of Dunning R 3327 AT tumor
520

Tumor volume (mm^3)	Tumor group	Whole tumor Akep	Rim Akep	Average No. of rim CSI voxels	Core Akep	Average no. of core CSI voxels
110-265	I	1.59±0.53	1.61±0.52	6	0.15±0.14	1
478-649	II	0.65±0.12	0.71±0.12	10	0.27±0.07	3
1035-1207	III	0.55±0.11	0.63±0.12	11	0.36±0.12	6
1409-1708	IV	0.36±0.04	0.50±0.07	12	0.15±0.03	8
1941-2453	V	0.34±0.05	0.47±0.07	14	0.14±0.02	10

Lactate imaging and DCE-MRI in prostate tumors

521   Table 2B Average Akep values of Dunning H tumors
522

523

Tumor volume (mm^3)	Tumor group	Whole tumor Akep	Rim Akep	Average no. of Rim CSI voxels	Core Akep	Average no. of Core CSI voxels
227-259	I	1.23±0.12	1.23±0.12	7	--	0
430-546	II	1.06±0.23	1.07±0.23	9	0.76±0.27	1
1000-1236	III	0.84±0.21	0.85±0.21	11	0.77±0.23	3
1382-1715	IV	0.86±.08	0.90±0.04	13	0.75±0.19	7
1886-2255	V	0.46±.04	0.53±0.05	12	0.38±.06	11

Lactate imaging and DCE-MRI in prostate tumors

Figure 1a

Figure 1b

Figure 1

Lactate imaging and DCE-MRI in prostate tumors

Figure 2

Lactate imaging and DCE-MRI in prostate tumors
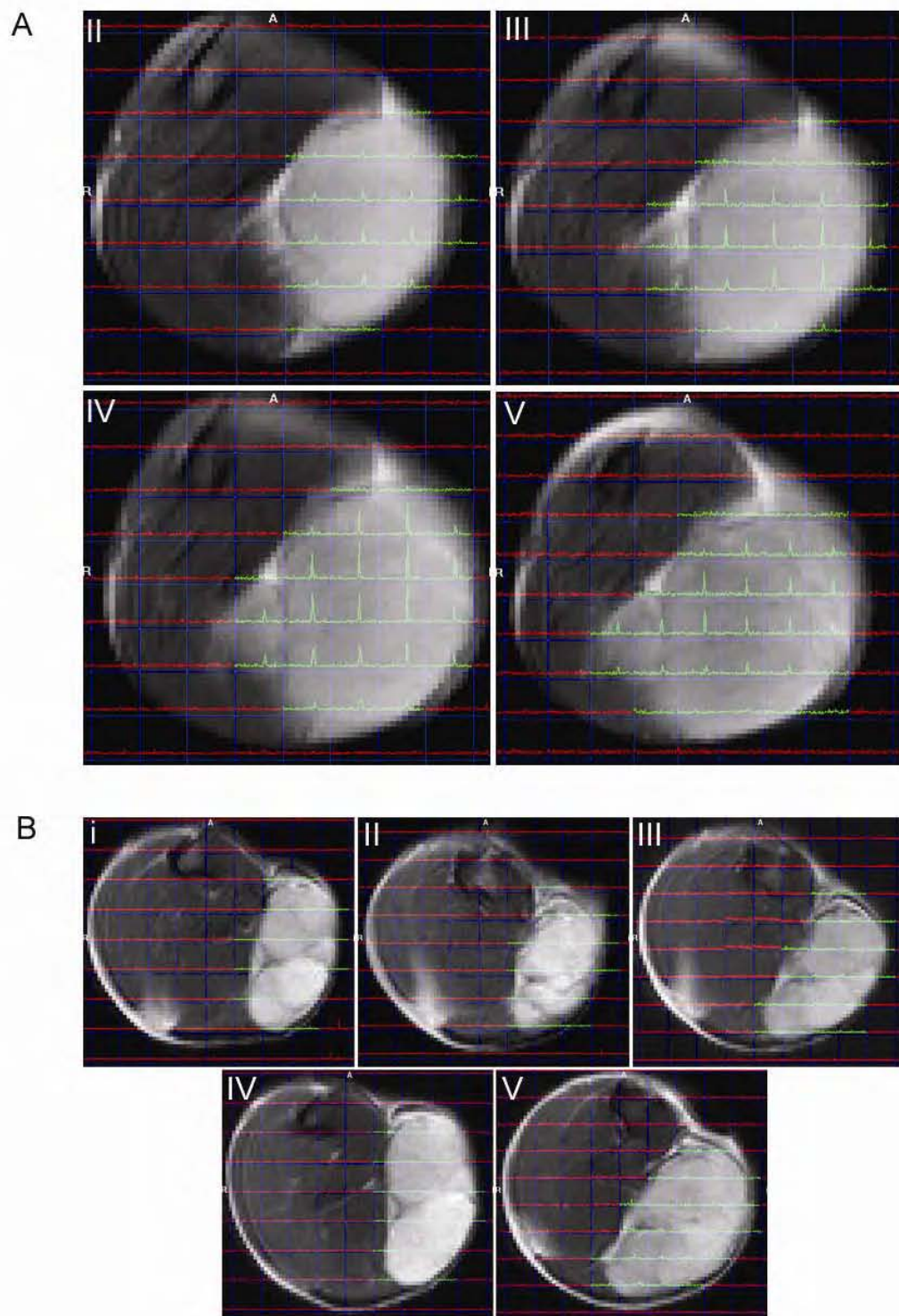
Figure 3A

Figure 3B

Figure 3

Lactate imaging and DCE-MRI in prostate tumors
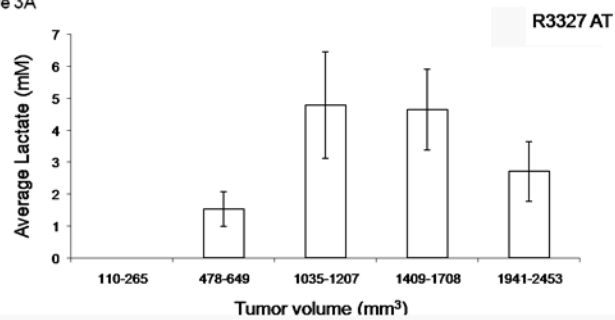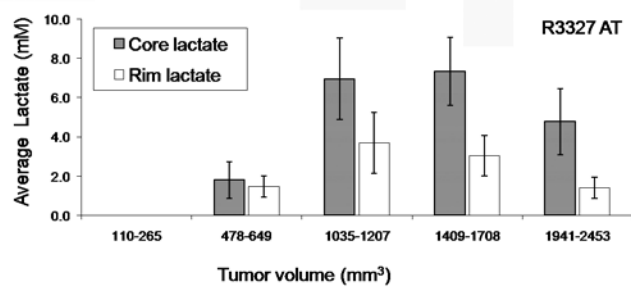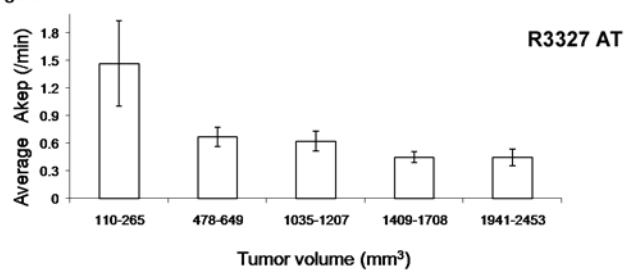
Figure 4A

Figure 4B

Figure 4

527

Lactate imaging and DCE-MRI in prostate tumors

Figure 5A

Dunning H

Figure 5B

Dunning H

Core Akep
Rim Akep

Figure 5

528

Lactate imaging and DCE-MRI in prostate tumors

529
530 Figure 6

Lactate imaging and DCE-MRI in prostate tumors
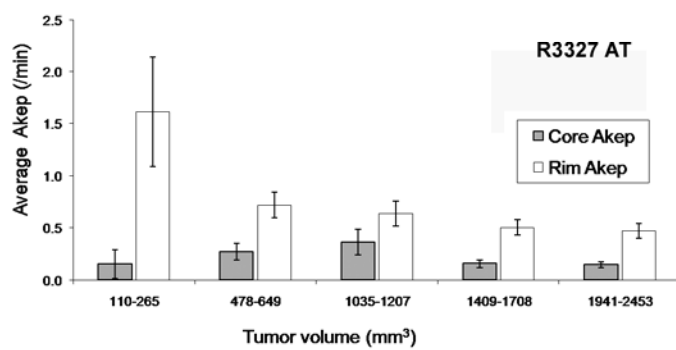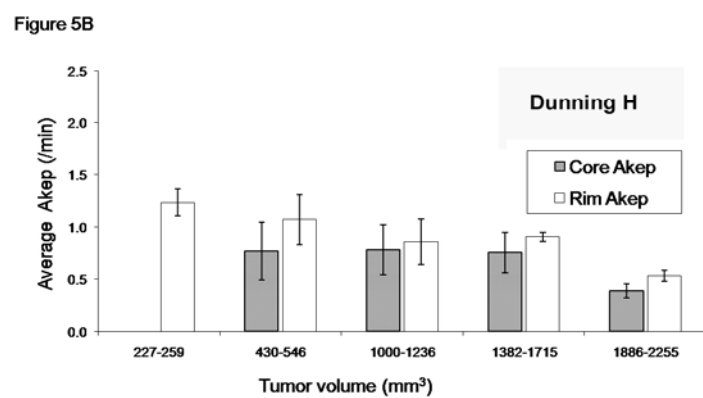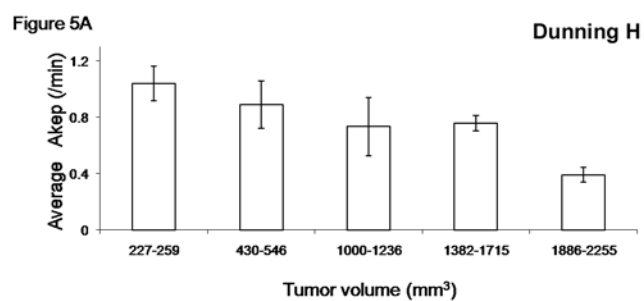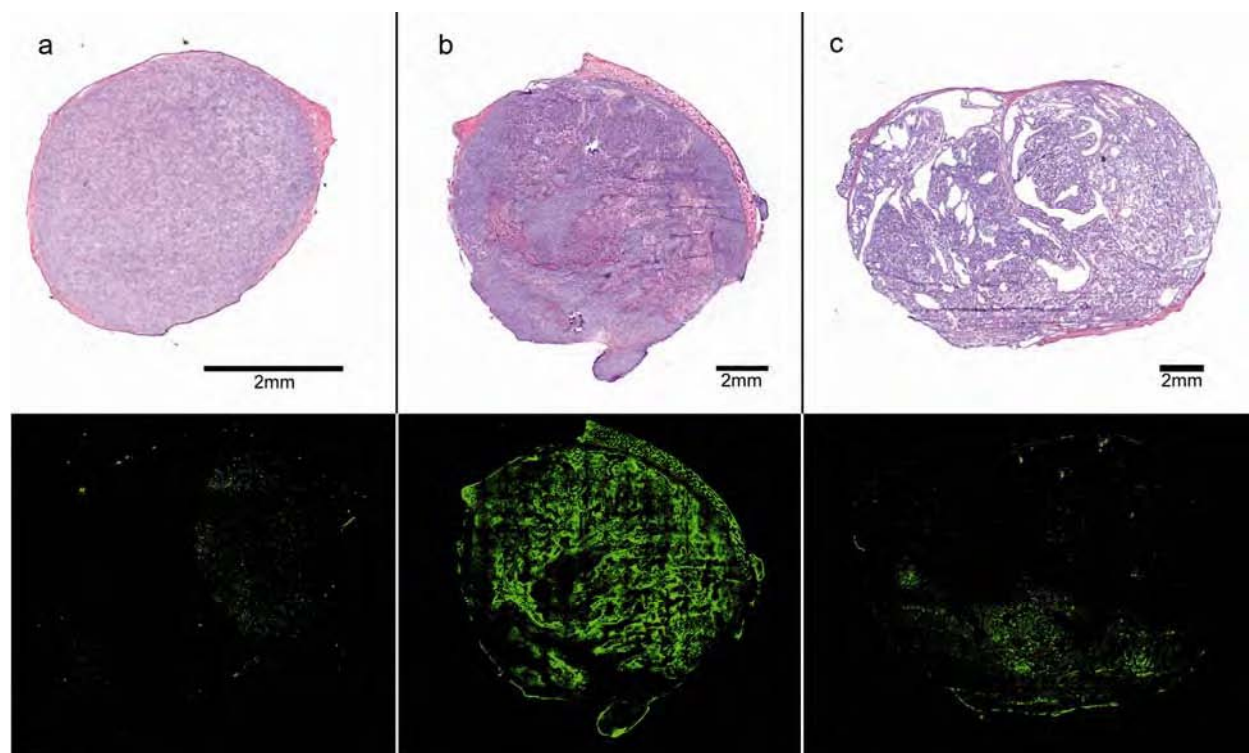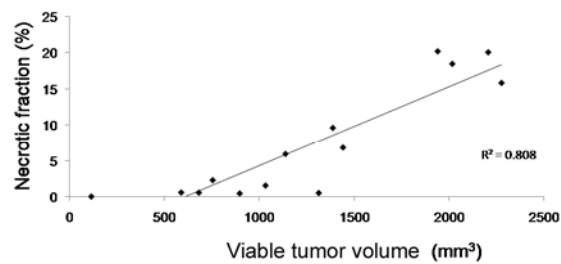
Figure 7A

Figure 7B

Figure 7C

Figure 7

531

Lactate imaging and DCE-MRI in prostate tumors

532 **References**

533 [1] Miller DC, Gruber SB, Hollenbeck BK, Montie JE, and Wei JT (2006). Incidence of

534   initial local therapy among men with lower-risk prostate cancer in the United States.

535   *Journal of the National Cancer Institute* **98**, 1134-1141.

536 [2] Cooperberg MR, Lubeck DP, Meng MV, Mehta SS, and Carroll PR (2004). The changing

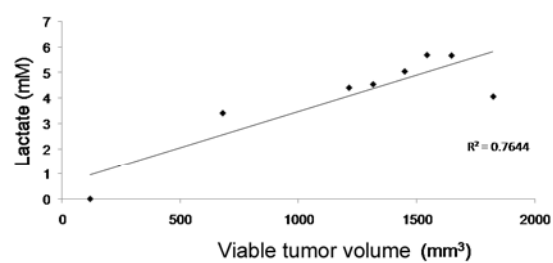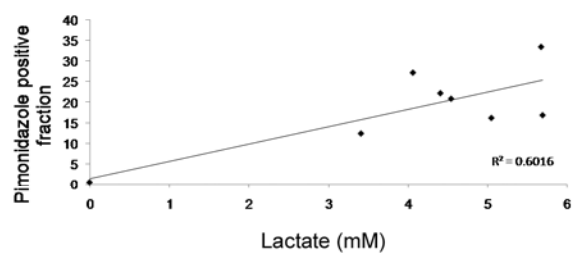537   face of low-risk prostate cancer: trends in clinical presentation and primary management.

538   *J Clin Oncol* **22**, 2141-2149.

539 [3] Chun FK, Karakiewicz PI, Huland H, and Graefen M (2007). Role of nomograms for

540   prostate cancer in 2007. *World J Urol* **25**, 131-142.

541 [4] Steyerberg EW, Roobol MJ, Kattan MW, van der Kwast TH, de Koning HJ, and Schroder

542   FH (2007). Prediction of indolent prostate cancer: validation and updating of a prognostic

543   nomogram. *J Urol* **177**, 107-112; discussion 112.

544 [5] Nowell PC (1976). The clonal evolution of tumor cell populations. *Science* **194**, 23-28.

545 [6] Gao C, Furge K, Koeman J, Dykema K, Su Y, Cutler ML, Werts A, Haak P, and Vande

546   Woude GF (2007). Chromosome instability, chromosome transcriptome, and clonal

547   evolution of tumor cell populations. *Proc Natl Acad Sci U S A* **104**, 8995-9000.

548 [7] Lang GA, Iwakuma T, Suh YA, Liu G, Rao VA, Parant JM, Valentin-Vega YA, Terzian

549   T, Caldwell LC, Strong LC, *et al.* (2004). Gain of function of a p53 hot spot mutation in a

550   mouse model of Li-Fraumeni syndrome. *Cell* **119**, 861-872.

551 [8] Perryman LA, Blair JM, Kingsley EA, Szymanska B, Ow KT, Wen VW, MacKenzie KL,

552   Vermeulen PB, Jackson P, and Russell PJ (2006). Over-expression of p53 mutants in

553   LNCaP cells alters tumor growth and angiogenesis in vivo. *Biochem Biophys Res*

554   *Commun* **345**, 1207-1214.

555 [9] Okawa T, Michaylira CZ, Kalabis J, Stairs DB, Nakagawa H, Andl CD, Johnstone CN,

556   Klein-Szanto AJ, El-Deiry WS, Cukierman E*, et al.* (2007). The functional interplay

557   between EGFR overexpression, hTERT activation, and p53 mutation in esophageal

558   epithelial cells with activation of stromal fibroblasts induces tumor development,

559   invasion, and differentiation. *Genes Dev* **21**, 2788-2803.

560 [10]   Lowe SW, Ruley HE, Jacks T, and Housman DE (1993). p53-dependent apoptosis

561   modulates the cytotoxicity of anticancer agents. *Cell* **74**, 957-967.

562 [11]   Li G, Bush JA, and Ho VC (2000). p53-dependent apoptosis in melanoma cells after

563   treatment with camptothecin. *J Invest Dermatol* **114**, 514-519.

564 [12]   Ling CC, Humm J, Larson S, Amols H, Fuks Z, Leibel S, and Koutcher JA (2000).

565   Towards multidimensional radiotherapy (MD-CRT): biological imaging and biological

566   conformality. *International journal of radiation oncology, biology, physics* **47**, 551-560.

567 [13]   Walenta S, Wetterling M, Lehrke M, Schwickert G, Sundfor K, Rofstad EK, and

568   Mueller-Klieser W (2000). High lactate levels predict likelihood of metastases, tumor

569   recurrence, and restricted patient survival in human cervical cancers. *Cancer research*

570   **60**, 916-921.

571 [14]   Walenta S, Salameh A, Lyng H, Evensen JF, Mitze M, Rofstad EK, and Mueller-Klieser

572   W (1997). Correlation of high lactate levels in head and neck tumors with incidence of

573   metastasis. *The American journal of pathology* **150**, 409-415.

574 [15]   Bhujwalla ZM, and Glickson JD (1996). Detection of tumor response to radiation

575   therapy by in vivo proton MR spectroscopy. *International journal of radiation oncology,*

576   *biology, physics* **36**, 635-639.

577 [16]   Aboagye EO, Bhujwalla ZM, Shungu DC, and Glickson JD (1998). Detection of tumor

578   response to chemotherapy by 1H nuclear magnetic resonance spectroscopy: effect of 5-

579   fluorouracil on lactate levels in radiation-induced fibrosarcoma 1 tumors. *Cancer*

580   *research* **58**, 1063-1067.

581 [17]   Kurhanewicz J, and Vigneron DB (2008). Advances in MR spectroscopy of the prostate.

582   *Magn Reson Imaging Clin N Am* **16**, 697-710, ix-x.

583 [18]   Joseph T, McKenna DA, Westphalen AC, Coakley FV, Zhao S, Lu Y, Hsu IC, Roach

584   M, 3rd, and Kurhanewicz J (2009). Pretreatment endorectal magnetic resonance imaging

585   and magnetic resonance spectroscopic imaging features of prostate cancer as predictors

586   of response to external beam radiotherapy. *International journal of radiation oncology,*

587   *biology, physics* **73**, 665-671.

588 [19]   Yeh KA, Biade S, Lanciano RM, Brown DQ, Fenning MC, Babb JS, Hanks GE, and

589   Chapman DC (1995). Polarographic needle electrode measurements of oxygen in rat

590   prostate carcinomas: accuracy and reproducibility. *International journal of radiation*

591   *oncology, biology, physics* **33**, 111-118.

592 [20]   Thorndyke C, Meeker BE, Thomas G, Lakey WH, McPhee MS, and Chapman JD

593   (1985). The radiation sensitivities of R3327-H and R3327-AT rat prostate

594   adenocarcinomas. *J Urol* **134**, 191-198.

595 [21]   Zhao D, Ran S, Constantinescu A, Hahn EW, and Mason RP (2003). Tumor oxygen

596   dynamics: correlation of in vivo MRI with histological findings. *Neoplasia* **5**, 308-318.

597 [22]   Rothman DL, Behar KL, Hetherington HP, and Shulman RG (1984). Homonuclear 1H

598   double-resonance difference spectroscopy of the rat brain in vivo. *Proc Natl Acad Sci U S*

599   *A* **81**, 6330-6334.

600   [23]   Nosel W, Trimble LA, Shen JF, and Allen PS (1989). On the use of double-quantum

601   coherence from an AX3 system (protons in lactate) for spectral editing. *Magn Reson Med*

602   **11**, 398-404.

603   [24]   Hurd RE, and Freeman D (1991). Proton editing and imaging of lactate. *NMR in*

604   *biomedicine* **4**, 73-80.

605   [25]   He Q, Shungu DC, van Zijl PC, Bhujwalla ZM, and Glickson JD (1995). Single-scan in

606   vivo lactate editing with complete lipid and water suppression by selective multiple-

607   quantum-coherence transfer (Sel-MQC) with application to tumors. *Journal of magnetic*

608   *resonance* **106**, 203-211.

609   [26]   Danielsen ER, Michaelis T, and Ross BD (1995). Three methods of calibration in

610   quantitative proton MR spectroscopy. *Journal of magnetic resonance* **106**, 287-291.

611   [27]   Hoffmann U, Brix G, Knopp MV, Hess T, and Lorenz WJ (1995). Pharmacokinetic

612   mapping of the breast: a new method for dynamic MR mammography. *Magn Reson Med*

613   **33**, 506-514.

614   [28]   Naressi A CC, Cstang I, Beer R. de, Graveron-Demilly D, (2001) in *Computers in biology*

615   *and medicine*, p. 269.

616   [29]   Muruganandham M, Koutcher JA, Pizzorno G, and He Q (2004). In vivo tumor lactate

617   relaxation measurements by selective multiple-quantum-coherence (Sel-MQC) transfer.

618   *Magn Reson Med* **52**, 902-906.

619   [30]   Cho H, Ackerstaff E, Carlin S, Lupu ME, Wang Y, Rizwan A, O'Donoghue J, Ling CC,

620   Humm JL, Zanzonico PB, *et al.* (2009). Noninvasive multimodality imaging of the tumor

621   microenvironment: registered dynamic magnetic resonance imaging and positron

622   emission tomography studies of a preclinical tumor model of tumor hypoxia. *Neoplasia*

623   **11**, 247-259, 242p following 259.

624   [31]   Brizel DM, Schroeder T, Scher RL, Walenta S, Clough RW, Dewhirst MW, and

625   Mueller-Klieser W (2001). Elevated tumor lactate concentrations predict for an increased

626   risk of metastases in head-and-neck cancer. *International journal of radiation oncology,*

627   *biology, physics* **51**, 349-353.

628   [32]   Walenta S, Chau TV, Schroeder T, Lehr HA, Kunz-Schughart LA, Fuerst A, and

629   Mueller-Klieser W (2003). Metabolic classification of human rectal adenocarcinomas: a

630   novel guideline for clinical oncologists? *Journal of cancer research and clinical*

631   *oncology* **129**, 321-326.

632   [33]   Cornel EB, Smits GA, Oosterhof GO, Karthaus HF, Deburyne FM, Schalken JA, and

633   Heerschap A (1993). Characterization of human prostate cancer, benign prostatic

634   hyperplasia and normal prostate by in vitro 1H and 31P magnetic resonance

635   spectroscopy. *J Urol* **150**, 2019-2024.

636   [34]   Swanson MG, Zektzer AS, Tabatabai ZL, Simko J, Jarso S, Keshari KR, Schmitt L,

637   Carroll PR, Shinohara K, Vigneron DB*, et al.* (2006). Quantitative analysis of prostate

638   metabolites using 1H HR-MAS spectroscopy. *Magn Reson Med* **55**, 1257-1264.

639   [35]   Tessem MB, Swanson MG, Keshari KR, Albers MJ, Joun D, Tabatabai ZL, Simko JP,

640   Shinohara K, Nelson SJ, Vigneron DB*, et al.* (2008). Evaluation of lactate and alanine as

641   metabolic biomarkers of prostate cancer using 1H HR-MAS spectroscopy of biopsy

642   tissues. *Magn Reson Med* **60**, 510-516.

643   [36]   Chen AP, Albers MJ, Cunningham CH, Kohler SJ, Yen YF, Hurd RE, Tropp J, Bok R,

644   Pauly JM, Nelson SJ*, et al.* (2007). Hyperpolarized C-13 spectroscopic imaging of the

645   TRAMP mouse at 3T-initial experience. *Magn Reson Med* **58**, 1099-1106.

646   [37]   Albers MJ, Bok R, Chen AP, Cunningham CH, Zierhut ML, Zhang VY, Kohler SJ,

647   Tropp J, Hurd RE, Yen YF*, et al.* (2008). Hyperpolarized 13C lactate, pyruvate, and

648   alanine: noninvasive biomarkers for prostate cancer detection and grading. *Cancer*

649   *research* **68**, 8607-8615.

650   [38]   Chen C, Pore N, Behrooz A, Ismail-Beigi F, and Maity A (2001). Regulation of glut1

651   mRNA by hypoxia-inducible factor-1. Interaction between H-ras and hypoxia. *J Biol*

652   *Chem* **276**, 9519-9525.

653   [39]   Minchenko O, Opentanova I, and Caro J (2003). Hypoxic regulation of the 6-

654   phosphofructo-2-kinase/fructose-2,6-bisphosphatase gene family (PFKFB-1-4)

655   expression in vivo. *FEBS Lett* **554**, 264-270.

656   [40]   Papandreou I, Cairns RA, Fontana L, Lim AL, and Denko NC (2006). HIF-1 mediates

657   adaptation to hypoxia by actively downregulating mitochondrial oxygen consumption.

658   *Cell Metab* **3**, 187-197.

659   [41]   Kim JW, Tchernyshyov I, Semenza GL, and Dang CV (2006). HIF-1-mediated

660   expression of pyruvate dehydrogenase kinase: a metabolic switch required for cellular

661   adaptation to hypoxia. *Cell Metab* **3**, 177-185.

662   [42]   Lin Z, Mechalakos J, Nehmeh S, Schoder H, Lee N, Humm J, and Ling CC (2008). The

663   influence of changes in tumor hypoxia on dose-painting treatment plans based on 18F-

664   FMISO positron emission tomography. *International journal of radiation oncology,*

665   *biology, physics* **70**, 1219-1228.

666 [43]   Rajendran JG, Hendrickson KR, Spence AM, Muzi M, Krohn KA, and Mankoff DA

667   (2006). Hypoxia imaging-directed radiation treatment planning. *Eur J Nucl Med Mol*

668   *Imaging* **33 Suppl 1**, 44-53.

669 [44]   Shappley WV, 3rd, Kenfield SA, Kasperzyk JL, Qiu W, Stampfer MJ, Sanda MG, and

670   Chan JM (2009). Prospective Study of Determinants and Outcomes of Deferred

671   Treatment or Watchful Waiting Among Men With Prostate Cancer in a Nationwide

672   Cohort. *J Clin Oncol*.

673 [45]   Shukla-Dave A, Hricak H, and Scardino PT (2008). Imaging low-risk prostate cancer.

674   *Curr Opin Urol* **18**, 78-86.

675 [46]   Adalsteinsson E, Spielman DM, Pauly JM, Terris DJ, Sommer G, and Macovski A

676   (1998). Feasibility study of lactate imaging of head and neck tumors. *NMR in*

677   *biomedicine* **11**, 360-369.

678 [47]   Pan JW, Hamm JR, Hetherington HP, Rothman DL, and Shulman RG (1991).

679   Correlation of lactate and pH in human skeletal muscle after exercise by 1H NMR. *Magn*

680   *Reson Med* **20**, 57-65.

681 [48]   Graham GD, Blamire AM, Howseman AM, Rothman DL, Fayad PB, Brass LM, Petroff

682   OA, Shulman RG, and Prichard JW (1992). Proton magnetic resonance spectroscopy of

683   cerebral lactate and other metabolites in stroke patients. *Stroke* **23**, 333-340.

684
685
686
687
688
689
690
691
692